Master's Thesis

Development of GEM detectors for a large acceptance lepton pair spectrometer

February 8, 2010

Department of Physics, Graduate School of Science, University of Tokyo

Yosuke Watanabe

Contents

1 Introduction **1**

2 J-PARC E16 experiment **9**
2.1 Overview . . . 9
2.2 Spectrometer design . . . 10

3 Prototype of GEM tracker **15**
3.1 Brief view of a GEM tracker . . . 15
3.2 Mechanical structure . . . 17
3.3 Readout . . . 20
3.4 Gas . . . 20
3.5 High voltage distribution . . . 21

4 Laboratory test **23**
4.1 Evaluation properties . . . 23
4.1.1 Property of a triple-GEM configuration . . . 23
4.1.2 Double-side readout board . . . 24
4.2 Test of a triple-GEM configuration . . . 24
4.2.1 Effective gain . . . 24
4.2.2 Collection efficiency . . . 26
4.2.3 Transverse diffusion constant . . . 32
4.3 Test of a double-side readout board . . . 37
4.3.1 Signal shape . . . 37
4.3.2 Charge sharing between top and bottom sides . . . 37

5 Beamtest **39**
5.1 Evaluation properties . . . 39
5.2 Tested setup . . . 42
5.2.1 Beam . . . 42
5.2.2 Front End Electronics and DAQ . . . 42
5.2.3 Scintillator . . . 43
5.2.4 Silicon strip detector . . . 44
5.3 GEM handling in beam test . . . 48
5.4 Estimation of tracking accuracy . . . 48
5.5 Analysis results . . . 49
5.5.1 Pedestal run . . . 49

5.5.2 Data and analysis 50
5.5.3 Alignment of the GEM tracker to the SSDs 56
5.5.4 Total charge, S/N ratio and uniformity 56
5.5.5 Time calibration 56
5.5.6 Spatial resolution and efficiency 56

6 Conclusion **63**

Chapter 1

Introduction

The fundamental theory of strong interaction between quarks and gluons is known as Quantum Chromo Dynamics (QCD). One of main QCD feature is a running coupling constant [1, 2, 3, 4]. The running coupling constant means the coupling constant of QCD has a strong energy dependence. Figure 1.1 illustrates the running coupling constant as a function of energy scale. The coupling constant becomes weaker at high energy, which is called asymptotic freedom of QCD.

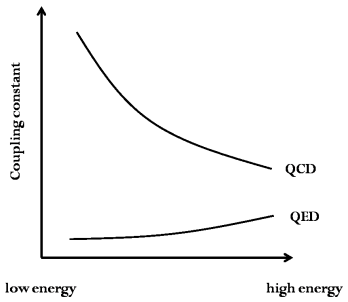

Figure 1.1: Coupling constant of QCD and QED as a function of energy scale

To know the origin of hadron mass, quantitative understanding QCD in low energy region is essential. At high energy, a perturbative method is successfully used to calculate physical quantity. However, at low energy, the method cannot be used due to the strong coupling constant.

Chiral symmetry is one of the most important aspects of QCD at low energy. Chiral transformation is defined as follows for one flavor quark.

$$\psi \rightarrow e^{-i\theta}\psi \tag{1.1}$$

$$\psi \rightarrow e^{-i\gamma_5\theta}\psi \tag{1.2}$$

The QCD Lagrangian is symmetric under those transformations in massless limit. The origin of hadronic mass is related to spontaneous breaking of the chiral symmetry, as proposed by Prof. Y. Nambu [5, 6]. When the spontaneous breaking of chiral symmetry occurs, quark and anti-quark pairs condense in the vacuum. The condensate interacts with

constituent quarks and generates their mass. In this context, π meson can be considered as a Nambu-Goldstone boson.

Breaking of symmetry can be characterized with an order parameter. The order parameter becomes 0 with a symmetric phase, while it becomes finite with a symmetry breaking phase. Quark condensates, $\langle\overline{q}q\rangle$, is widely-used as an order parameter for the chiral symmetry. The order parameter as a function of density and temperature is shown in Fig 1.2. The chiral symmetry, which is broken in the vacuum, is expected to restore at finite density and/or finite temperature.

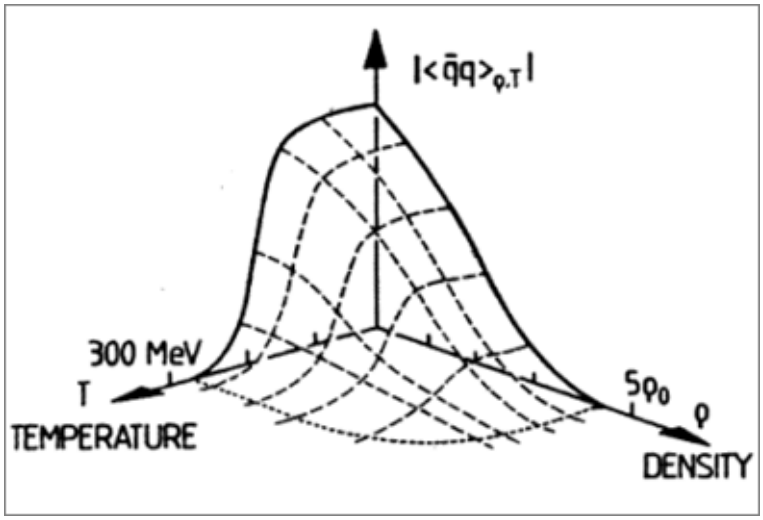

Figure 1.2: QCD phase diagram: An order parameter of chiral symmetry is drawn [7]

Establishing the change of quark condensates and investigating the origin of hadron mass is one of the most important experimental tasks in hadron physics. Mass spectra of hadrons in hot/dense medium can be a tool, because the spectra will reflect the intrinsic structure of the medium. This is in analogy with an electron in a solid, where the effective mass of an electron is heavier than the bare mass. The dispersion relation of an electron in a solid reflects the interaction between an electron and a solid

To investigate physics of hadrons, there are several theoretical efforts. Especially, QCD sum rule shows that the mass spectrum has to change in a QCD medium as a result of symmetry restoration. The constraint from the QCD sum rule is not strong enough to give unique shape of mass spectra. To describe the shape, many theoretical models are proposed such as chiral symmetry restoration [8, 9], many-body effects of hadron [10], mixing between vector and axial vector components [11].

Experimentally, light vector meson is used as a probe to search chiral symmetry restoration; such as CERES [12], NA60 [13], KEK-PS E325 [14, 15], J-Lab g7 [16], CBELSA/TAPS [17] and in SPring-8 LEPS [18]. Heavy ion collisions or nuclear reactions are used to generate a hot/dense medium. The in-medium mass of light vector mesons is reconstructed from decay products. For such purpose, lepton pair decays are suitable, since leptons do not have a final state interaction with the medium. The experiments except TAPS employ lepton-pair decay mode to measure the vector meson mass. However the lepton decay mode suffers a small branching ratio as shown in Table 1.1.

Table 1.1: Properties of vector mesons [4]

	Mass (MeV/c^2)	Γ(MeV/c^2)	$c\tau$ (fm)	Main decay	$\frac{\Gamma_{e^+e^-}}{\Gamma_{tot}}$ ($\times 10^{-5}$)
ρ^0	775.49	149.4	1.3	$\pi^+\pi^-$ ($\sim 100\%$)	4.7
ω	782.65	8.49	23.2	$\pi^+\pi^-\pi^0$ (89%)	7.2
ϕ	1019.455	4.26	46.2	K^+K^- (49%)	29.7

All the experiments agree that mass spectra of light vector mesons are modified in hot/dense medium [19, 20]. Most of the experiments claim broadenings of vector mesons. However, KEK-PS E325 claims mass shifts. Details of KEK-PS E325 and J-Lab g7 results are shown below.

KEK-PS E325

The invariant mass spectra of e^+e^- pairs produced in a nuclear reaction, $p + A \rightarrow X + \rho/\omega/\phi$, was investigated at the KEK 12GeV Proton Synchrotron. The setup is shown in Fig 1.3. This experiment is designed to cover a rapidity range of $0.5 < y < 2.0$ to detect slowly moving ϕ mesons. The spectrometer consists of two arms having drift chambers, Cherenkov detectors, time-of-flight counters and electromagnetic calorimeters. The spectrometer achieved a pion rejection power of 3×10^{-4} and mass resolution of ~ 10MeV.

To see the nuclear size dependence of mass spectra, two types of targets, carbon and copper, are used. Mass spectra with different $\beta\gamma$ range for copper and carbon target are shown in Fig 1.4. The mass spectra are fitted with resonance shape of $\phi \rightarrow e^+e^-$ and quadratic background shape. Although the carbon data and copper data with $\beta\gamma > 1.25$ are well reproduced by the fit, the copper data with $\beta\gamma < 1.25$ have excess on low-mass side of ϕ. Assuming the density dependence of ϕ meson mass as $m(\rho)/m(0) = 1 - k_1(\rho/\rho_0)$, k_1 is estimated to be $\sim 0.034^{+0.006}_{-0.007}$.

A mass spectrum of wide mass range for copper target is shown in Fig 1.5. The combinatorial background and the contributions of $\eta \rightarrow e^+e^-\gamma$ and $\omega \rightarrow e^+e^-\pi^0$ were already subtracted. The shape of combinatorial background was estimated with an event-mixing method and the normalization factor was determined by fitting to the invariant mass spectra excluding the range from 0.6 to 0.76 GeV. Like ϕ meson case, assuming the density dependence of ρ and ω meson mass as $m(\rho)/m(0) = 1 - k_1(\rho/\rho_0)$, k_1 is estimated to be $\sim 0.092 \pm 0.002$.

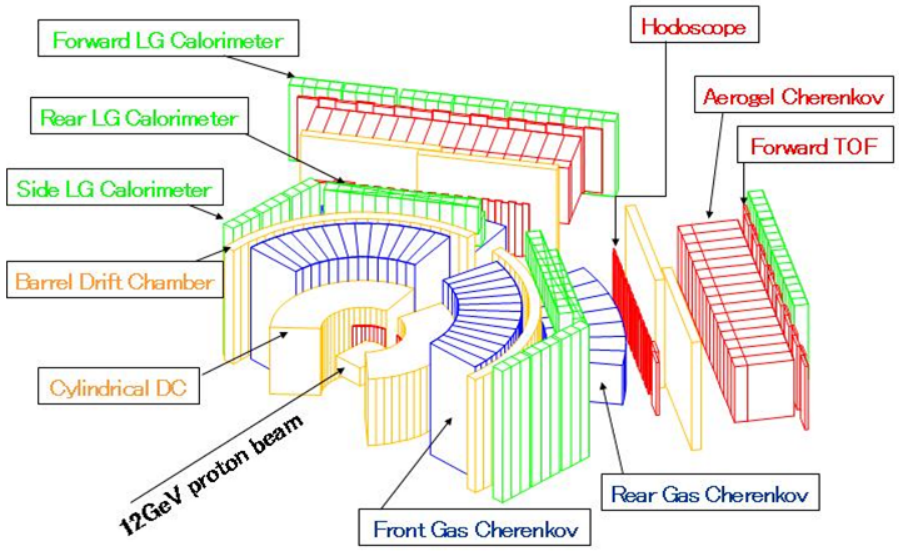

Figure 1.3: A setup of E325 experiment

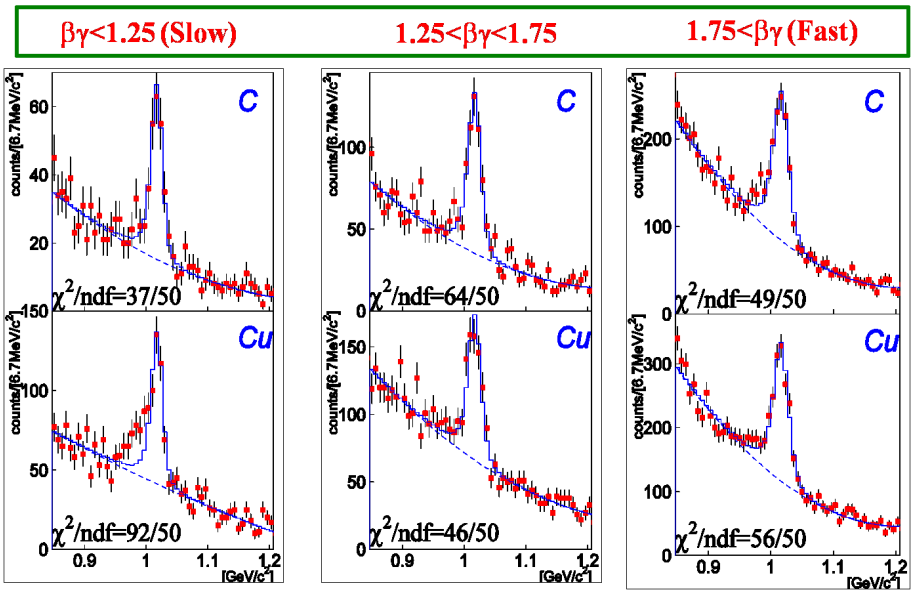

Figure 1.4: A result from E325 experiment: Clear excess is observed for slowly moving meson in Copper target [15]

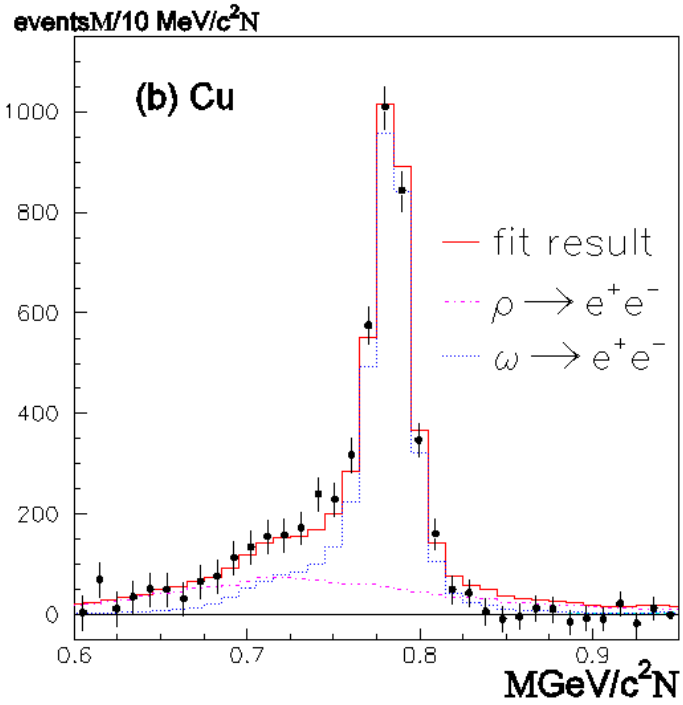

Figure 1.5: A result from E325 experiment [14]

J-Lab g7

The invariant mass spectra of e^+e^- are also measured with the CEBAF Large Acceptance Spectrometer (CLAS) at Jefferson Laboratory using $\gamma + A$ reactions. The incident beam was a tagged photon beam with energy of $0.6 \sim 3.8$GeV. The experiment used electromagnetic interaction in both the production and decay channels.

The setup is shown in Fig 1.6. The spectrometer is designed to track charged particles with momenta larger than 200MeV/c and covering almost the full solid angle. The spectrometer consists of six identical sectors having drift chambers, time-of-flight counters, Cherenkov counters and electromagnetic calorimeters. The pion rejection factor was 5.4×10^{-4} and the mass resolution was ~ 10MeV.

After the combinatorial background is subtracted, the mass spectra for ^{2}H, C and Fe-Ti targets are shown in Fig 1.7. The shape of combinatorial background was estimated with an event-mixing method and the normalization factor was determined by the number of observed like-sign pairs. By fitting the background-subtracted spectrum with Monte Carlo simulation, ρ mass shape was extracted from the spectra. As a result, k_1 is estimated to be 0.02 ± 0.02. The results of J-Lab g7 and KEK-PS E325 are different and the origin of the difference is still under investigation.

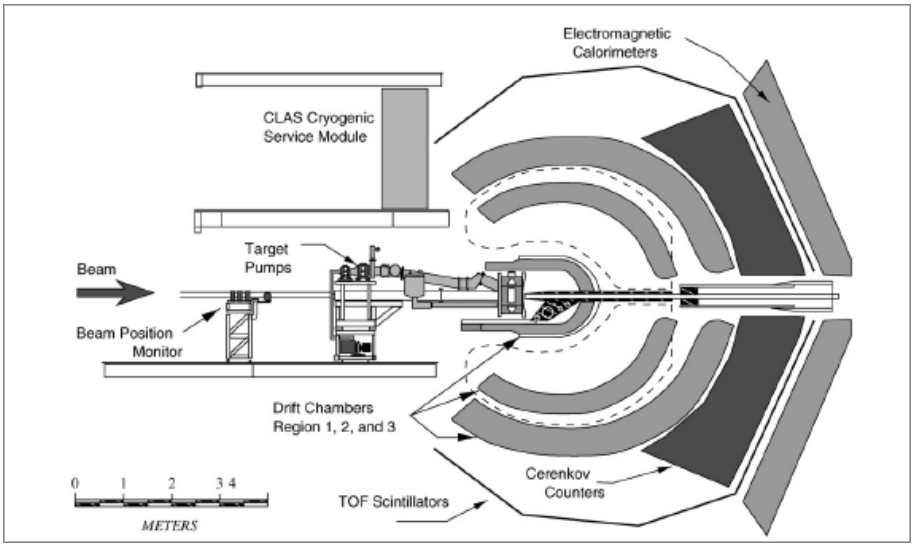

Figure 1.6: A setup of the g7 experiment [21]

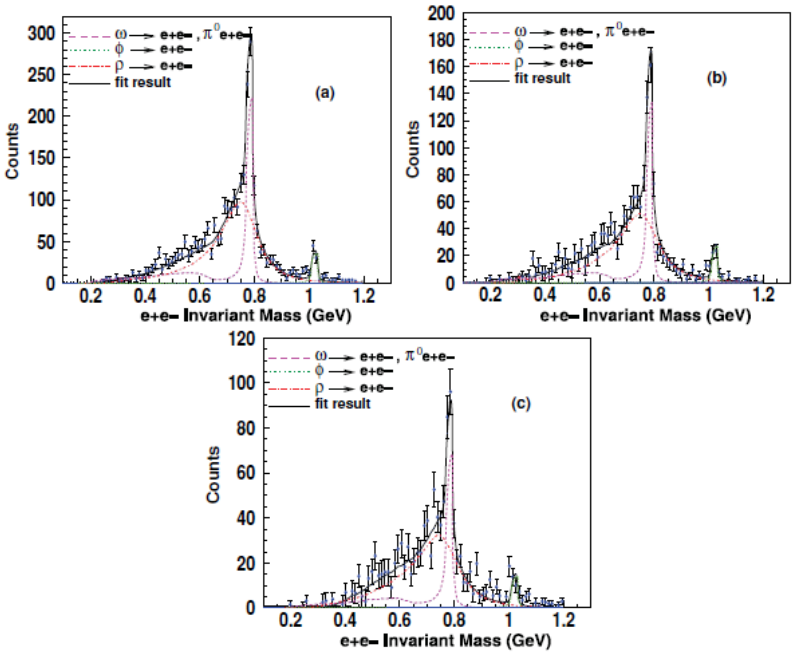

Figure 1.7: Results of the fits to the e^+e^- invariant mass spectrum obtained for the (a)^{2}H, (b) C and (c) Fe-Ti data [16].

Chapter 2

J-PARC E16 experiment

2.1 Overview

The main purpose of the J-PARC E16 experiment is to measure mass spectra in nuclear medium with high precision and high statistics [22].

Improvement in statistics from KEK-PS E325 experiment gives us an opportunity for using new targets. Targets of E325 and E16 are shown in Table 2.1. The targets are kept thin to reduce radiation tail. Pb and CH_2 targets can be used in addition to E325 targets. Large nucleus such as Pb enhances the possibility of vector meson's decaying inside, which is critical for the measurement of mass spectrum in the nuclear matter. Subtraction of C from CH_2 target gives the spectra of proton target. Expected spectra for Pb and proton are shown in Fig 2.1. The proton data can be used to subtract non-modified ϕ meson mass spectrum in the spectrum of larger target nuclei. Thus, the in-medium invariant mass spectra is obtained in a model-independent way. In addition, with higher statistics, dependence of meson velocity can be studied in more details. Thus, the dispersion relation of ϕ meson in the nuclear medium can be studied more accurately.

To have the sensitivity to mass shift, a mass resolution is also important. The effect of experimental invariant mass resolution on the modified ϕ meson mass distribution is shown in Fig 2.2. The result shows that 10 MeV in r.m.s. at the ϕ mass is needed to keep the same level as KEK-PS E325.

The statistics will be improved from KEK-PS E325 in the following way.

1. 10 times higher beam intensity
2. 5 times larger acceptance
3. 2 times higher cross section

The first and the second things in the above list are realized with a new spectrometer. In KEK-PS E325, spectrometer's rate capability limited by a beam intensity. New developed detectors, which has high rate capability, enable us to have experiment with higher intensity beam at J-PARC.

The spectrometer is placed at the focus point of high momentum beam line as shown in Fig 2.3. Primary proton of 30 GeV is delivered to the beamline and beam intensity of 10^{10}/spill is needed for the experiment.

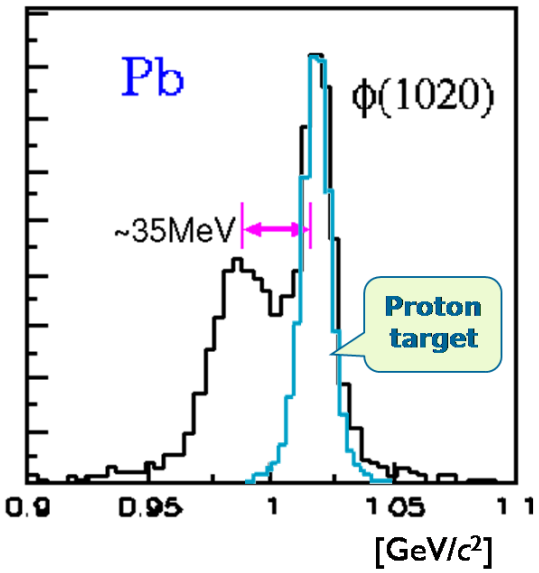

Figure 2.1: An expected spectrum in J-PARC E16 experiment.

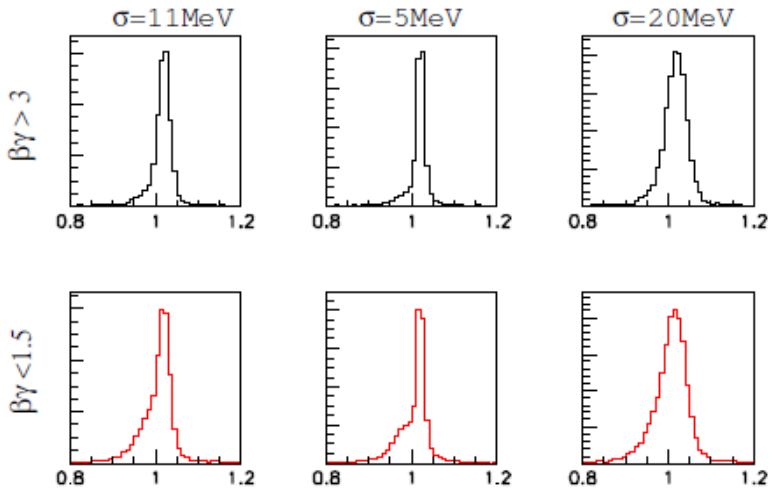

Figure 2.2: The expected modified invariant mass distributions of $\phi \to e^+e^-$ from Cu target with different experimental mass resolutions. Upper panels show the spectra by fast moving mesons and lowers show by slowly moving mesons.

2.2 Spectrometer design

Proposed spectrometer covers backward in CM system to detect slowly moving mesons which has higher probability of decaying inside nuclei. Schematic view of the spectrometer is shown in Fig 2.4. The acceptance of the spectrometer is 0°-135° in horizontal and −45°-45° in vertical. The very forward region of −12°-12° both vertically and horizontally is

Table 2.1: Targets of E325 and E16

	Material	Thickness	Radiation length	Interaction length
E325	Cu	81μm	0.57%	0.054%
	C	81μm	0.43%	0.21%
E16	Pb	20μm	0.3%	0.01%
	Cu	80μm	0.5%	0.05%
	CH_2	400μm	0.1%	0.05%
	C	200μm	0.1%	0.05%

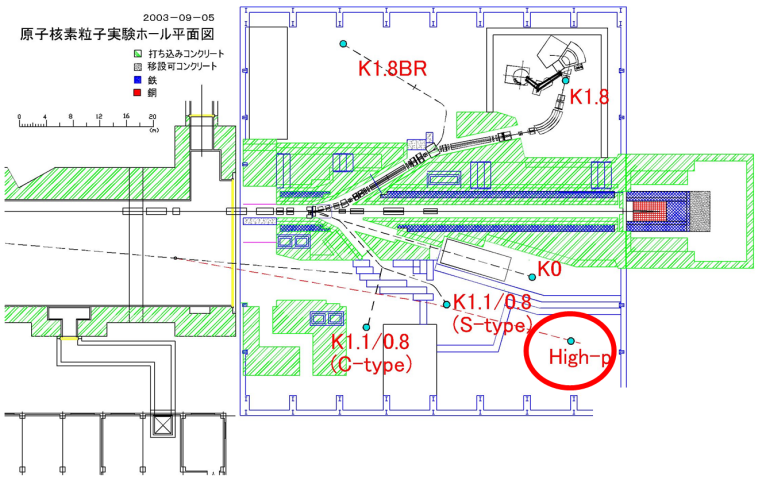

Figure 2.3: Hadron hall in J-PARC: the high momentum beamline needs to be constructed

removed to avoid beam halo.

The spectrometer consists of tracking detectors and electron identification detectors.

Electron and positron identification

To perform high precision measurements, high purity of electron detection is essential. The spectrometer needs to have a high rejection factor of other charged particles. The combination of Hadron Blind Detector (HBD) and the Lead Glass calorimeter establish the rejection factor of 10000. Photograph and schematic view of HBD is shown in Fig 2.5.

Tracker

Momenta of electrons and positrons are mainly determined by three layers of GEM trackers in a magnetic field. That is the minimum number of points to determine the momenta of a traversing particle.

Expected momentum resolution of J-PARC E16 for various spatial resolutions is shown in Fig 2.6. The momentum resolution achieved in KEK-PS E325 is also shown as the solid line. The required spatial resolution for the GEM tracker is 100μm, which gives the momentum resolution of $\sim$ 5MeV. We need to achieve 100μm for tracks of incident angle

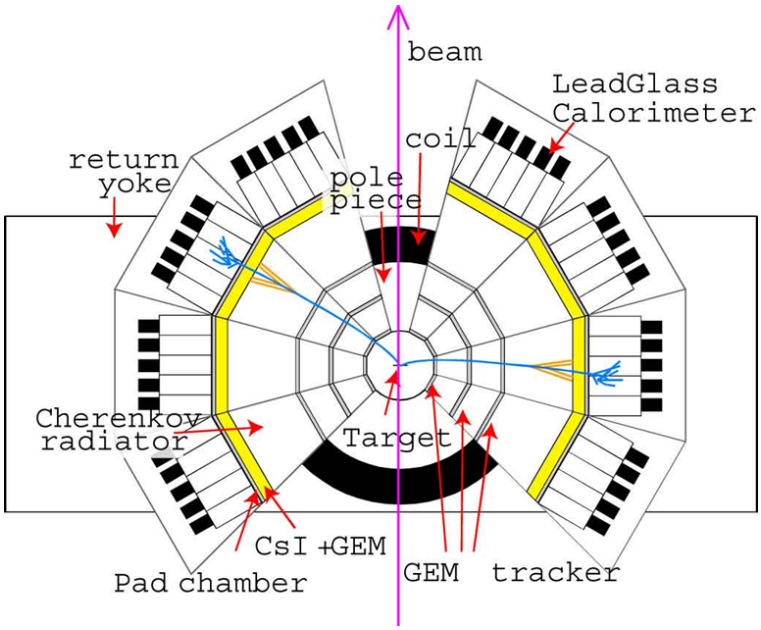

Figure 2.4: The schematic view of spectrometer

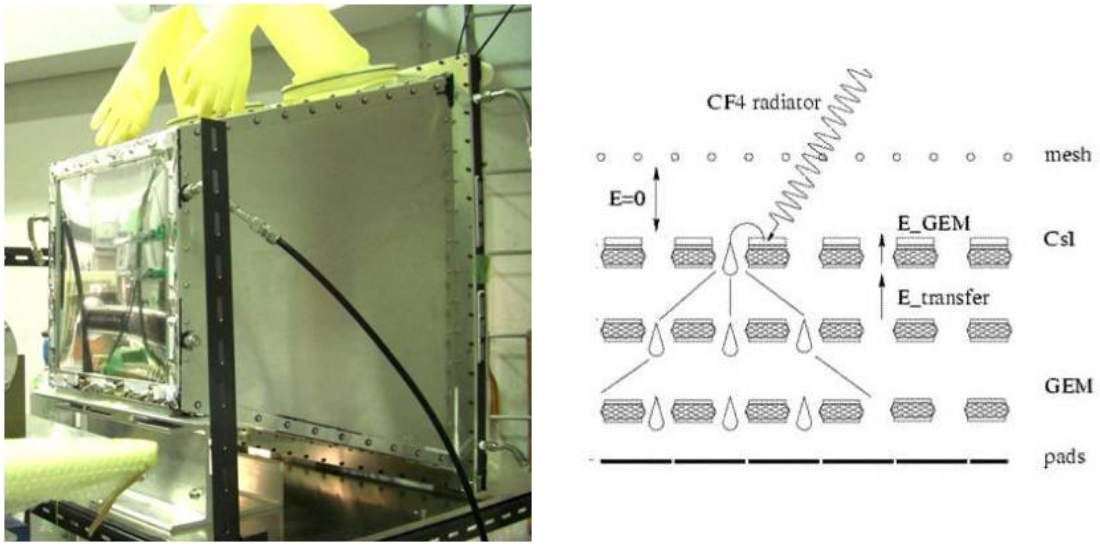

Figure 2.5: Photograph and schematic view of Hadron Blind Detector

of 0° to 30°. Even if particles go through radialy, the incident angle is expected to be 15° when they hit the edge of the GEM tracker.

The counting rate of the most inner tracker is estimated to be $\sim 5\text{kHz/mm}^2$. To cope with such high rate, Gas Electron Multipliers are used in the experiment.

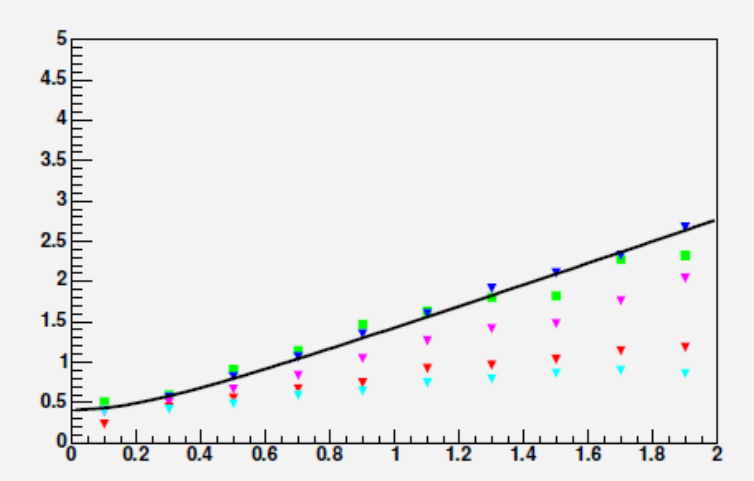

Figure 2.6: Momentum resolution ($\delta p/p$) as a function of momentum for E325(green), spatial resolution of 300 μm (blue),200 μm(purple), 100μm (red), 50 μm (cyan). Black line represents achieved momentum resolution for E325

Chapter 3

Prototype of GEM tracker

A photograph and a schematic view of a GEM tracker is shown in Fig 3. From the top, a drift electrode, three Gas Electron Multiplier (GEM) foils and a two-dimensional readout board are placed. In this manuscript we call the setup with three GEM foils as a triple-GEM configuration. The gaps between GEM foils and a drift electrode are called drift gap, transfer gap 1, transfer gap 2 and induction gap as shown in Fig 3.1.

The overview of a GEM detector is shown at first, and then a prototype tracker is described.

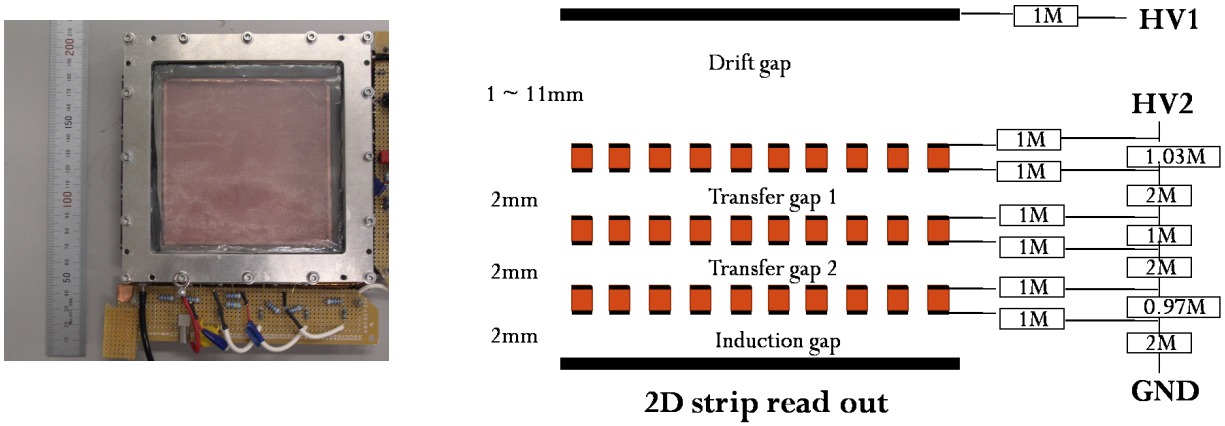

Figure 3.1: A photograph and a schematic view of the prototype GEM tracker

3.1 Brief view of a GEM tracker

Gas Electron Multiplier (GEM) is originally developed at CERN [23]. A GEM foil consists of an insulator and two thin copper layers, and they have many small holes. Figure 3.2 shows an example of a GEM foil. The design of a GEM foil for the prototype chamber is summarized in Fig 3.3. Design of a standard GEM foil at CERN is also shown.

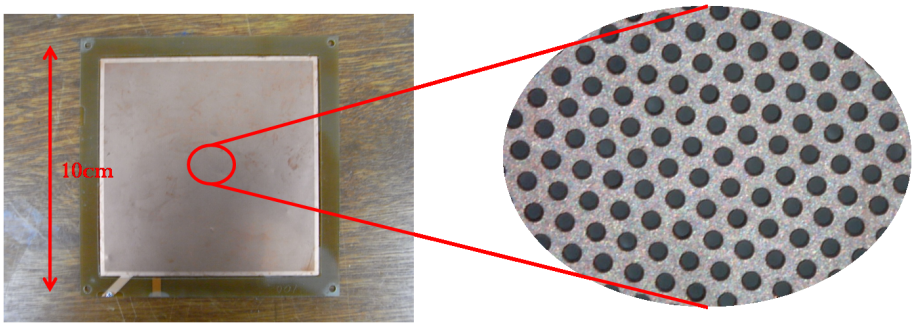

Figure 3.2: A picture of 100mm × 100mm GEM

	R_{PI}	R_{Cu}	P	D	d
Prototype	45	75	140	50	4
CERN	60	70	140	50	5

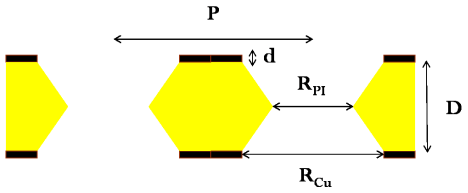

Figure 3.3: Design of a GEM foil used in a prototype tracker

By applying a suitable voltage between two copper layers, strong electric field is formed in holes. When the foil is placed in suitable gas, the field multiplies the electrons. A gain of 20-40 is achieved by one foil. Design of GEM largely affects its property. Especially, characteristics of gain strongly depend on shape of hole. Using a wet etching method, the shape is double-conical.

In the prototype GEM tracker, three layers of GEM foils are used in cascade to obtain the overall gain of $\sim$ 10000. A signal of an incident charged particle is formed in the following steps:

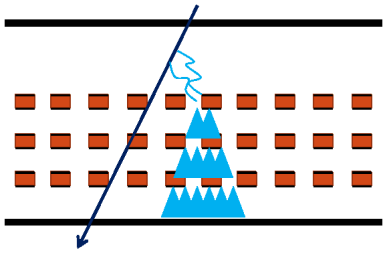

1. A charged particle ionizes gas molecules
2. The top GEM foil collects the electrons from the ionization
3. Three GEM foils multiply those electrons
4. A readout board collects amplified electrons

Advantages of GEM detectors are following. First, these detectors are capable of operating at higher rate than typical wire chamber, because of the fine hole pitch compared to the wire spacing. Second, the amplification region and a readout board can be separated. This separation allows us to use various readout geometries. Two-dimensional strip readout board is used in our case.

COMPASS experiment at CERN uses a triple-GEM configuration and two-dimensional strip readout board [24]. The configuration is almost the same as the prototype tracker. The GEM tracker in COMPASS achieves about 50μm spatial resolution with a strip pitch

of 400μm and is working up to 25kHz/mm^2. This rate capability satisfies our requirement [25].

3.2 Mechanical structure

Drawings of the prototype tracker are shown in Fig 3.4 and Fig 3.5. The chamber is designed to fulfill the following requirements:

1. Gas tightness

   Contamination of oxygen and water should be small, since oxygen and water, which are electronegative, capture electrons. Loss of electrons in drift gap results in worse spatial resolution.

   Gas tightness is realized with gas sealing made of viton. Since a setup inside the tracker is changed frequently in test, adhesives are not used in bonding.

2. Low material budget

   Since multiple scattering degrades momentum resolution of trackers, materials with small atomic number and minimum thickness need to be used. Components in the active area of the tracker and their radiation lengths are summarized in Table 3.1.

Component	Material	Length	Aperture ratio	Radiation length(per mil)
Lid	Myler	25 μm		0.0871
Catholde	Aluminized Myler	25 μm		0.0882
GEM1	Copper	8 μm	0.26	0.414
	Kapton	50 μm	0.17	0.146
	Total			0.56
GEM2				0.56
GEM3				0.56
Readout	Copper	4μm	0.8	0.0559
	Copper	4μm	0.171	0.232
	Kapton	25μm		0.0874
	Total			0.375
Total				2.53

Table 3.1: Radiation length of the sensitive area of the prototype chamber

A mesh sheet is also used as a cathode. Geometry and radiation length of the mesh sheet is summarized in Table 3.2. The setup with the mesh sheet has a radiation length of 2.98 per mil.

Table 3.2: Property of the mesh sheet used in the prototype tracker

Material	Thickness	Density	Radiation length
Stainless	50 μm	50 wire/inch	0.534

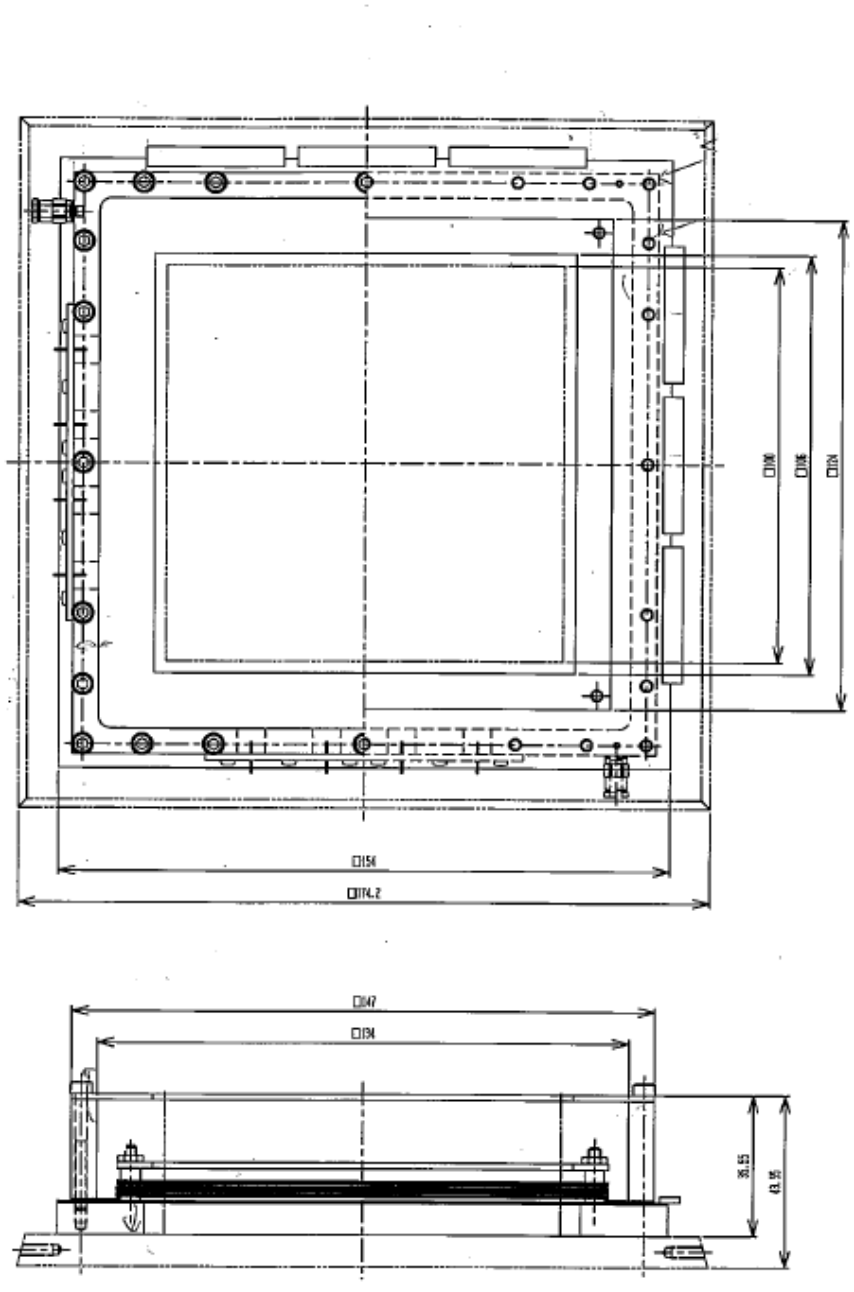

Figure 3.4: A drawing of the GEM tracker 1

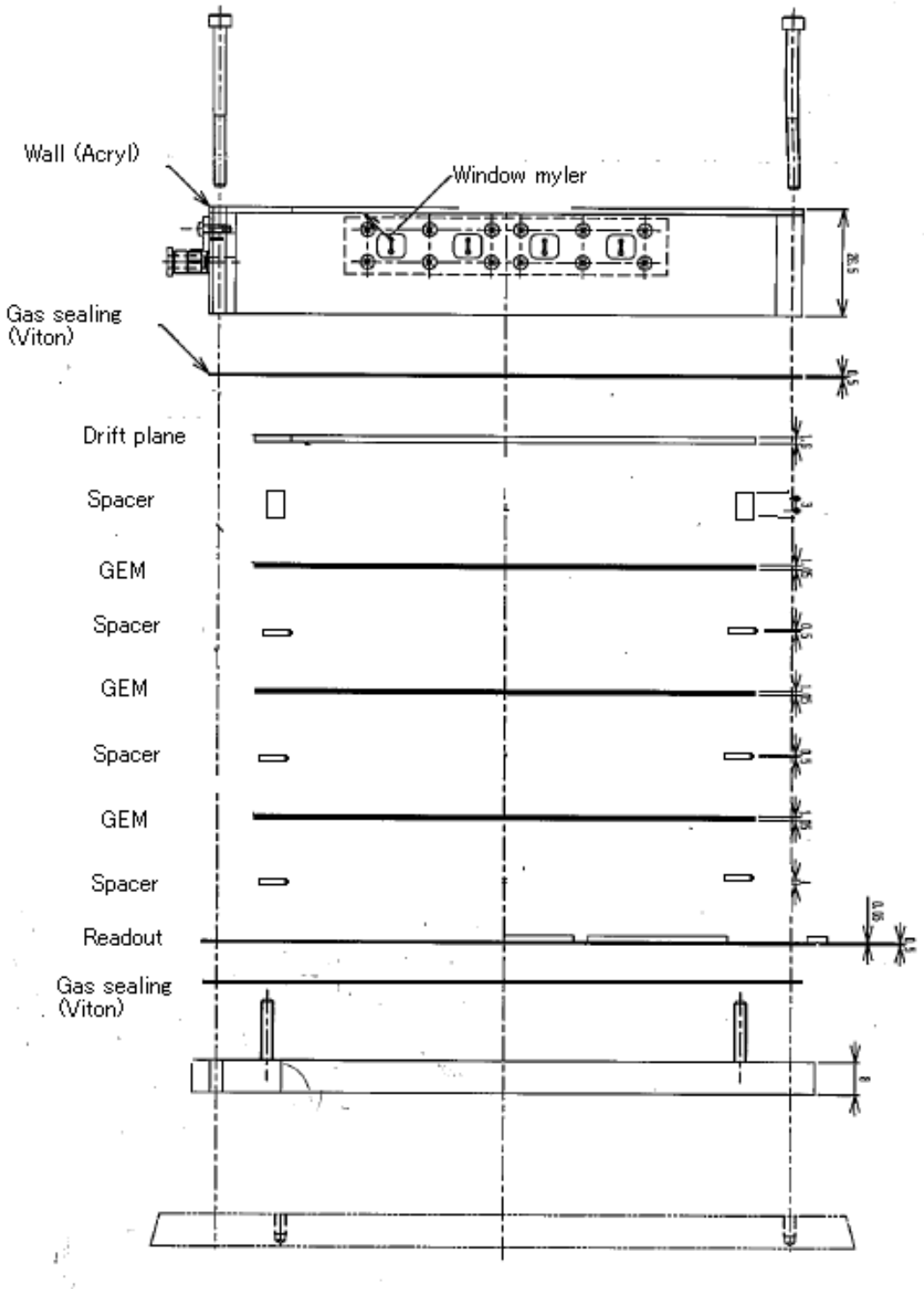

Figure 3.5: A drawing of the GEM tracker 2

3.3 Readout

Three types of readout boards are tested. Those readout boards are shown in Fig 3.3. The strip pitch and width are in common. The top strip width is 70μm, the bottom strip width is 290μm and the pitch is 350μm. Difference is the shape of insulator between the top and bottom strips. The insulator between the top strips is etched away in readout board 1. We call this board single-side. The insulator is not etched away for readout board 2 and 3. The bottom strips cannot be directly seen from the top side. This type is called double-side. For readout 1 and 2, two neighboring strips are connected and effective pitch of 700μm is obtained.

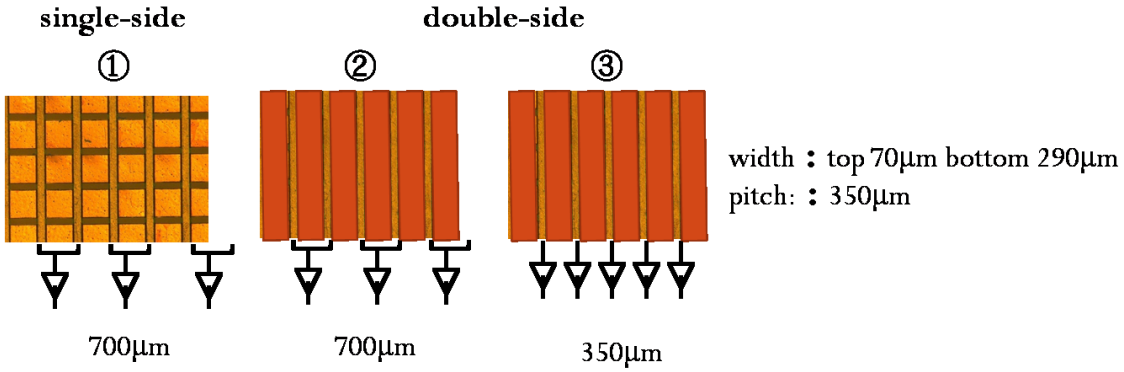

The readout strips are connected to preamplifiers with a connector and and a cable, which are shown in Fig 3.6 and Fig 3.7. The connector is wire-bonded to the strips. The cable consists of thin co-axial cables for each channel.

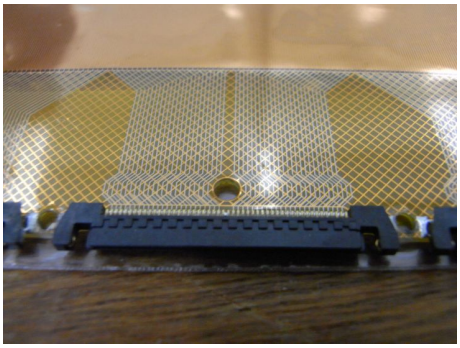

Figure 3.6: A connector of readout

Figure 3.7: A cable

3.4 Gas

Two types of gases are considered for the prototype tracker:

- Ar70%, $CO_2$30%
- Ar90%, $CH_4$10% (Often denoted as P10)

In both cases, the tracker is operated at atmospheric pressure.

The schematic view of a gas system is shown in Fig 3.8. The system consists of a gas cylinder, a gas reducing valve, a gas flow meter, the prototype tracker, a bubbler. They are connected with 1/4-inch nylon tube. Gas flow rate is kept to $\sim$ 100 ml/min in operation.

A bubbler is placed after the tracker to prevent the back-flow of air. The bubbler is filled with silicone oil.

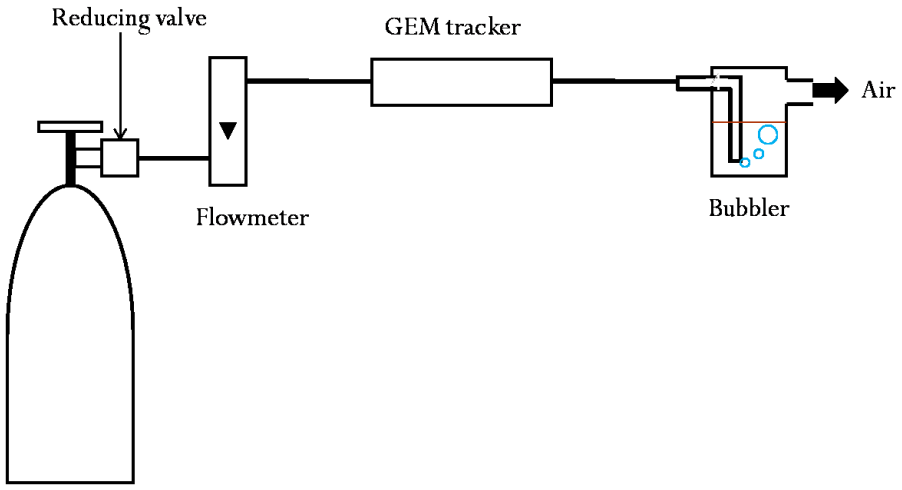

Figure 3.8: Gas system for the prototype tracker

3.5 High voltage distribution

A high voltage is applied to GEM foils using a resistive chain through protection resistors. Figure 3.9 shows two types of resistive chain used for laboratory tests and beam tests. The resistive chain in right panel applies high voltage asymmetrically to each GEM foil. The top GEM foil is operated with the highest voltage difference and the bottom GEM foil is operated with the lowest. Since the total charge of avalanche electrons becomes large at the bottom GEM foil, low voltage is preferable for the stable operation.

To vary the electric field of drift gap, HV supply is separated for the drift cathode.

Figure 3.9: Left: A resistive chain used in gain and collection efficiency measurement at Laboratory. Right: A resistive chain for the prototype tracker.

Chapter 4

Laboratory test

In this chapter, performance tests of a triple-GEM configuration and readout are described. The evaluation properties are shown at first, and then test results are described.

4.1 Evaluation properties

4.1.1 Property of a triple-GEM configuration

Spatial resolution of a tracker can be estimated by the following expression [26].

$$\sigma_{\mathrm{p}}^2 = \frac{1}{\mathrm{N_{eff}}}\Big(\frac{w^2}{12} + \mathrm{D}^2 \cdot \frac{\mathrm{d_D}}{2}\Big) + \Big(\frac{N}{S}\Big)^2 \cdot w^2 \tag{4.1}$$

where
- D — Diffusion constant in drift gap
- $\mathrm{N_{eff}}$ — Effective number of electrons in drift gap
- $\mathrm{d_D}$ — Drift gap size
- N/S — Noise vs signal ratio
- w — Strip pitch

Collection efficiency and effective gain

According to the model, we can see that the large value of $\mathrm{N_{eff}}$ and S are advantage for better spatial resolution. These values are related to effective gain and collection efficiency of GEM foils.

Collection efficiency ($\varepsilon_{\mathrm{col}}$) is defined as the fraction of generated electrons in drift gap that move to GEM holes for amplification. Not all the electrons in drift gap can enter holes, because some of them fall on the electrode of the top GEM foil or absorbed by water or oxygen contamination of the gas, as shown in Fig 4.1. The pulse height (PH) at readout board can be expressed as eq (4.2). Effective gain is defined as $\varepsilon_{\mathrm{col}} \times \mathrm{G}$.

$$\mathrm{PH} = \mathrm{N_{seed}} \times \varepsilon_{\mathrm{col}} \times \mathrm{G} \tag{4.2}$$

where
- $\mathrm{N_{seed}}$ — the number of electrons generated by a charged particle or X-ray
- G — Real gain

Note that the collection efficiency cannot be derived from a pulse height, since the pulse height is determined by the product of $\varepsilon_{\mathrm{col}}$ and G. In section 4.2, the collection efficiency

is derived using some models of signal formation. The measurements are performed only for P10.

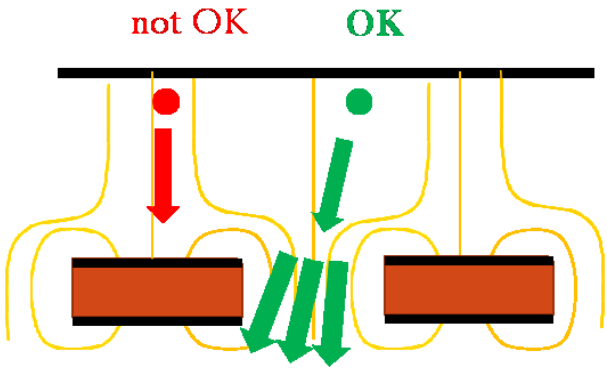

Figure 4.1: Electron motion in drift gap

Transverse diffusion constant

We can also see that transverse diffusion constant affects the spatial resolution. The transverse diffusion largely depends on the value of electric field. Since the diffusion constant in drift gap cannot be measured directly, the diffusion detected at readout is compared with that calculated with MAGBOLTZ simulation.

4.1.2 Double-side readout board

Single-side readout is already used in COMPASS experiment and equal charge sharing between the top side and the bottom side is realized. While, signal shape and pulse height should be checked carefully for a double-side readout board, because the bottom side cannot pick up electrons directly.

4.2 Test of a triple-GEM configuration

4.2.1 Effective gain

A measurement of effective gain is performed for Ar70%+$CO_2$30% and P10. Isotope of ^{55}Fe is used as an X-ray radiation source. Since X-ray deposites the fixed energy on average, X-ray is suitable for gain measurement of gas chamber. An example of energy spectrum detected by a GEM chamber is shown in Fig 4.2. The signal around 6keV corresponds to full energy deposit peak, and the one around 3keV corresponds to escape peak.

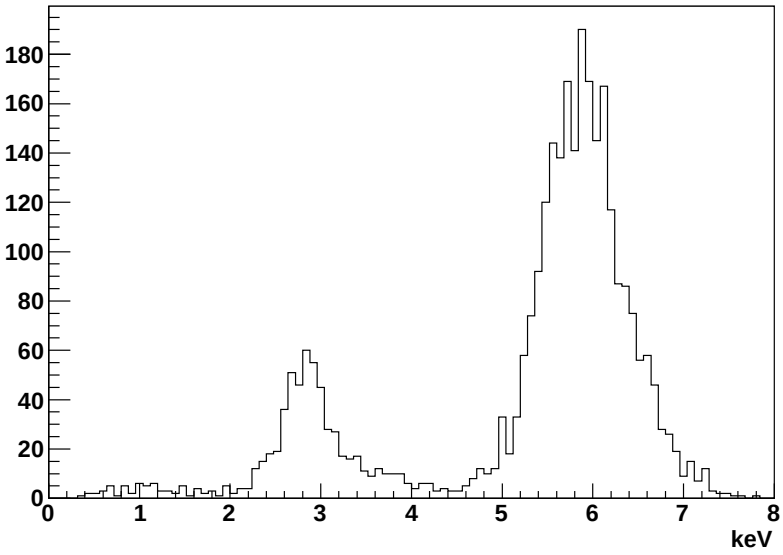

Figure 4.2: Energy spectrum of ^{55}Fe

Test setup

The chamber used in the test is shown in Fig 4.3. Pad readout is used for simplicity. The picture of the pad readout is also shown in Fig 4.3. A pad size is 16mm × 16mm, which is larger than a electron cloud. The typical size of a electron cloud is ∼ 1.5mm (FWHM) for P10.

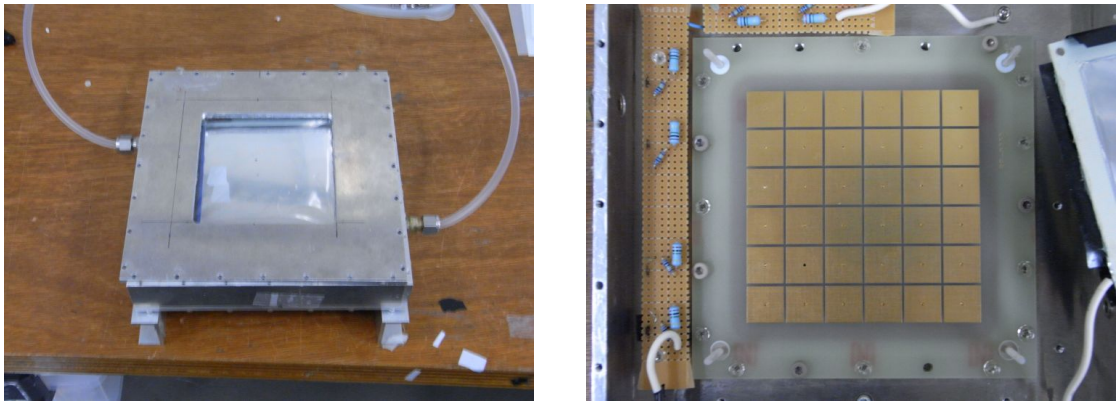

Figure 4.3: Left: A photograph of a test chamber Right: Inside of the test chamber

A charge-sensitive preamplifier is connected to a pad. A photograph and a schematic view of its electrical circuit is shown in Fig 4.4. The preamplifier consists of 2 stages amplification part. The first stage is charge-sensitive where 100kΩ resistor and 10pF capacitance are used as feedback. As a result, the time constant of the preamplifier is 1μsec. The second stage amplifies the signal by a factor of 10. The total gain of the preamplifier is 1V/pC. The output of the preamplifier is connected to oscilloscope.

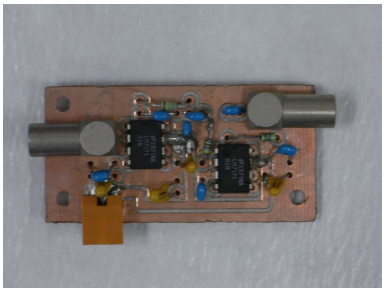

Figure 4.4: A photograph and a schematic view of the electrical circuit of the pre-amplifier

Result

Effective gain is calculated using obtained pulse height and known working energy of gas. Working energy of P10 and $ArCO_2$ is summarized in Table 4.1 [27]. Using thest numbers, 5.9keV X-ray generates 225 and 210 electrons in drift gap for P10 and $ArCO_2$, respectively.

$$\text{Pulse Height[mV]} = \frac{5900[\text{eV}]}{w[\text{eV}]} \times 1.6 \times 10^{-7} \times A \times 1000[\text{mV/pC}] \tag{4.3}$$

where A Effective gain
w Working energy

Table 4.1: Working energy of P10 and $ArCO_2$

P10	$ArCO_2$
26.2eV	28.1eV

The result of gain measurement is shown in Fig 4.5. The setup with $ArCO_2$ achieves higher gain than that with P10. The normal operation voltages of GEM foils for those gases are chosen as shown in table 4.2. The value is selected to have the gain $\sim$ 10000 and to be sufficiently lower than discharge voltage. When high voltage is supplied asymmetrically, the center GEM foil is operated with the value in the table.

P10	$ArCO_2$
340V	380V

Table 4.2: Operation voltage

4.2.2 Collection efficiency

Here, estimation of collection efficiency is performed using ^{90}Sr as a β radiation source. Collection efficiency is estimated through the following steps.

1. Measure energy spectrum experimentally

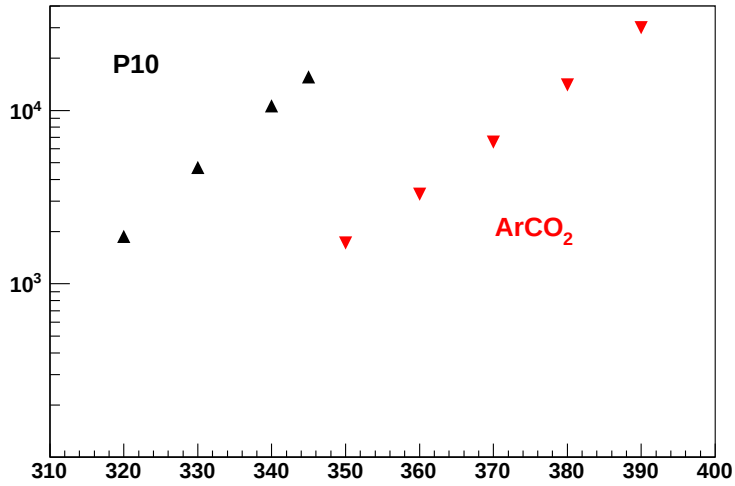

Figure 4.5: Comparing the gain of P10 and $ArCO_2$

2. Reproduce obtained energy spectrum with simulation of signal formation in a GEM chamber.

The test is performed only for P10.

Test setup

The chamber used in the gain measurement is also used here. A photograph and a schematic view of tested setup are shown in Fig 4.6. Isotope of ^{90}Sr emits electrons with energy less than 2MeV. Total 0.7MeV of energy loss occurs between the source and a trigger scintillation counter ,mainly due to the thickness of readout pad. As a result, electrons which reach the trigger scintillation counter has the energy above 0.7MeV. Electron signal with the energy 0.7MeV $\sim$ 2MeV can be observed in this setup. The bottom scintillation counter is placed for veto of cosmic ray.

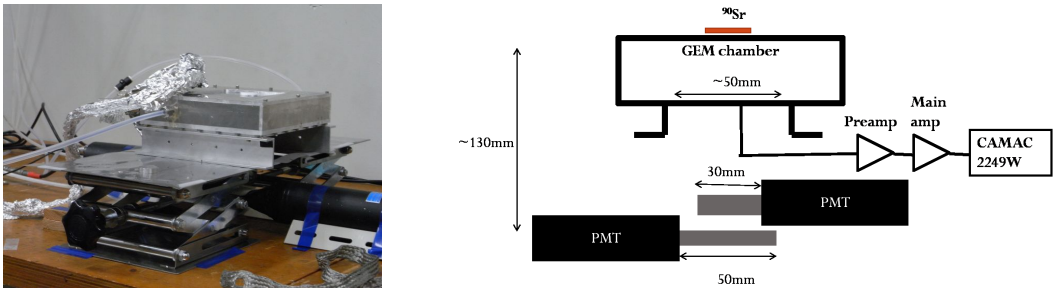

Figure 4.6: A photograph and a schematic view of its electrical circuit of the pre-amplifier

A preamplifier used in the test is shown in Fig 4.7, with the schematic view of the electrical circuit. A preamplifier has 16 channels. Gain of the preamplifier is $\sim$ 200mV/pC.

The preamplifier is connected to a main amplifier, whose gain is 10. The total gain of the circuit is 2V/pC.

Data acquisition system is built with Computer Automated Measurement And Control(CAMAC). A charge ADC (Lecroy2249W) is used for charge measurement. 2249W, charge ADC, is used for a readout of GEM chamber. The property of 2249W is summarized in Table 4.3. Trigger circuit is shown in Fig 4.8.

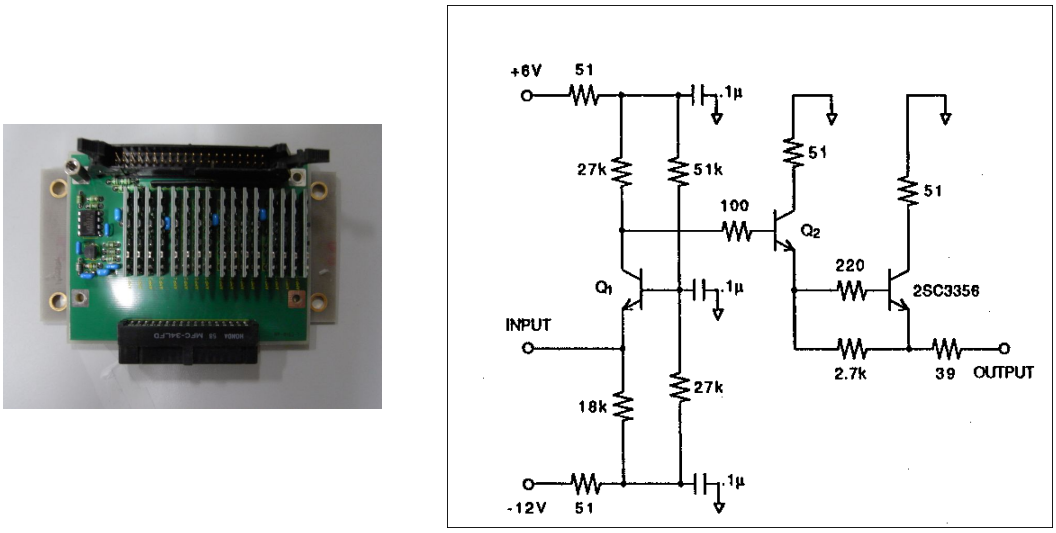

Figure 4.7: A photograph and a schematic view of the electrical circuit of the preamplifier [28]

Name	Conversion time	Full scale	Gain	Input impedance
2249W	106μsec	11bit	0.25pC/ch	50Ω

Table 4.3: Property of 2249W

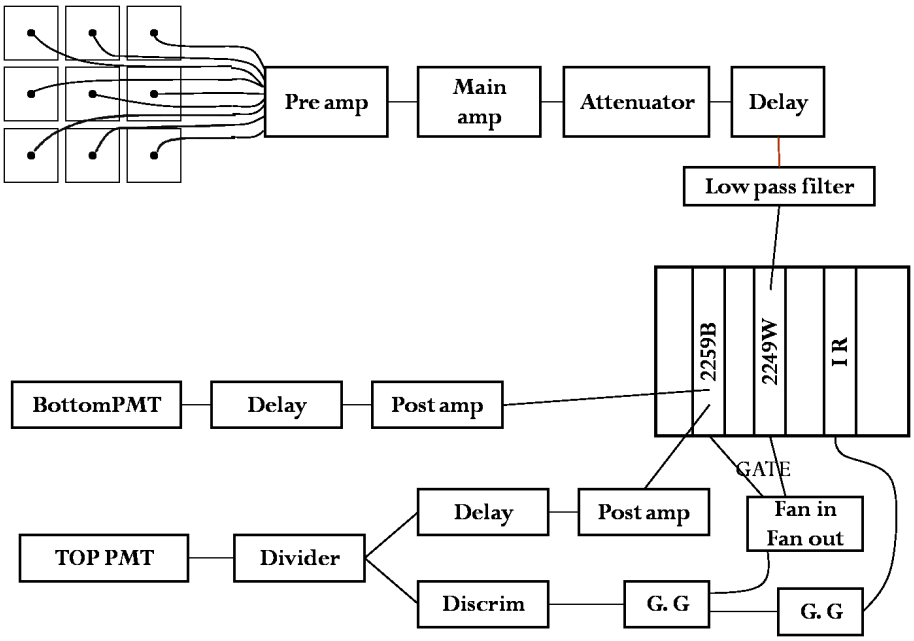

Figure 4.8: Trigger circuit

Experimental Result

An obtained spectrum is shown in Fig 4.9. For the spectrum, the events with hit on the center pad is selected.

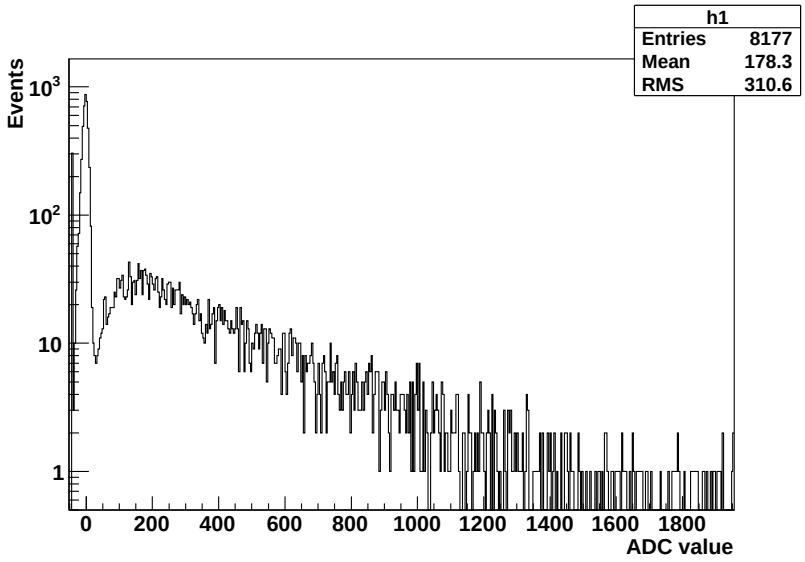

Figure 4.9: Spectrum of ^{90}Sr

Comparison with simulation

The signal of a triple-GEM configuration was simulated in the following steps.

1. Primary ionization

   The incident particle ionizes gas molecules. The mean number of primary electrons are assumed to be 26 electrons per cm. The Poisson statistic is used as shown in Fig 4.10.

2. Secondary ionization

   Some primary electrons are energetic enough to ionize gas molecules, and such electrons are forming a cluster. The distribution of cluster size is adopted from Table 2 of Ref [31] for argon. The distribution is shown in Fig 4.11.

3. Collection in the drift gap

   Collection efficiency is a free parameter. Here, the total number of electrons generated in 1. and 2. is multiplied by collection efficiency.

4. Amplification process by GEM

   Amplification factor can be approximated by polya distribution. Polya distribution is the following [30].

$$\frac{(1+\theta)^{(1+\theta)}}{\Gamma(1+\theta)}(\frac{q}{\overline{q}})^{(1+\theta)}exp(-(1+\theta)\frac{q}{\overline{q}}) \tag{4.4}$$

   where q Amplification factor
   $\overline{q}$ Mean amplification factor
   θ A free parameter to determine the shape of distribution

   Here, additional two free parameters arise: θ and $\overline{q}$.

   An example of polya function for various values of θ is shown in Fig 4.12. The sigma of this distribution is $\frac{1}{1+\theta}$. Experimental value of θ was not measured in previous. The appropriate value will be $0 \sim 3$ [29].

5. Amplification by readout circuit

6. Addition of noise

   Effect of noise is estimated from the experimental spectrum by fitting the pedestal peak with Gaussian. Effect of noise is added to the charge at step 5.

7. Addition of the events at pedestal

   Events in pedestal peak of the experimental spectrum correspond to dark current of trigger counter and inefficiency of the chamber. Here, the amount of pedestal peak in simulation is determined to match obtained spectrum.

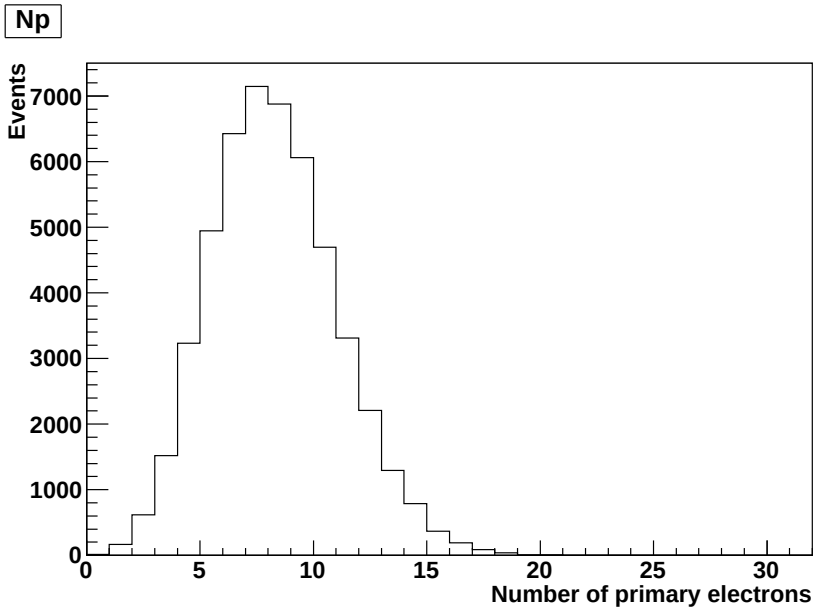

Figure 4.10: Simulation: Number of electrons ionized by incident charged particles. Poisson distribution is assumed.

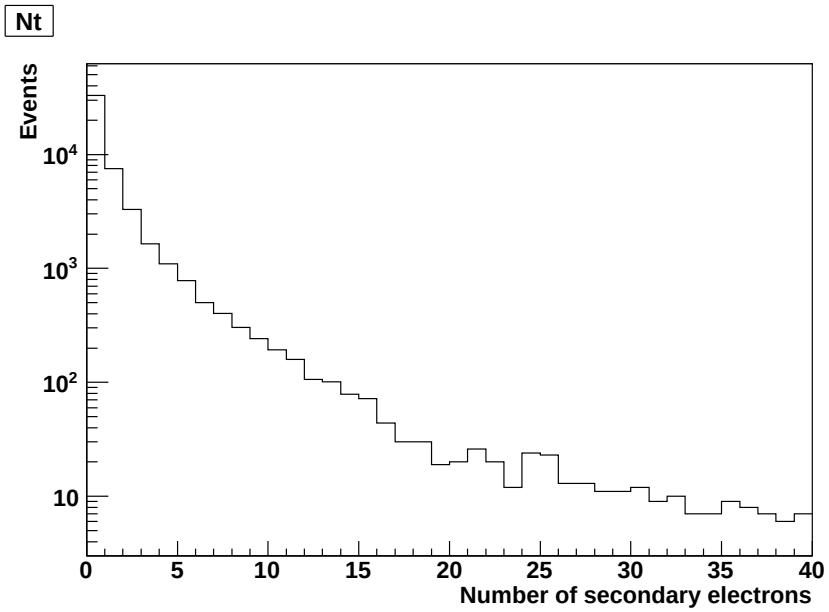

Figure 4.11: Cluster size distribution

In total, there are three free parameters in the simulation: $\varepsilon_{\rm col}$, $\overline{q}$ and θ.

The energy spectrum from simulation and experiment are compared by the following steps. First, an energy spectrum of simulation is normalized to have the same number of events from 20 to 400 in ADC value. Second, χ^2 is minimized by changing $\varepsilon_{\rm col}$, $\overline{q}$ and θ, with the minimum value of χ^2 is adopted as reasonable values of those free parameters.

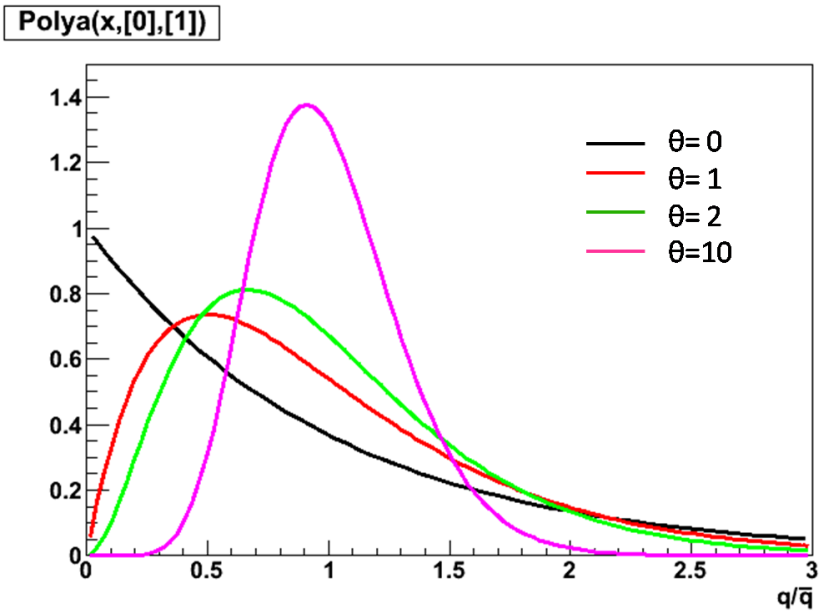

Figure 4.12: Polya function

$$\chi^2 = \sum_j \frac{(N^j_{sim} - N^j_{exp})^2}{N^j_{sim}} \tag{4.5}$$

where N^j_{sim} Number of events in j-th bin of simulated energy spectrum
N^j_{exp} Number of events in j-th bin of experimental energy spectrum

The typical parameters are summarized in Table 4.4, and the simulated spectrum is shown in Fig 4.13. However, when we take a collection efficiency above 0.5, we can reproduce the experimental spectrum with $\chi^2 < 1.5$. In conclusion, this method does not have enough sensitivity to know the collection efficiency above 0.5.

The simulated spectrum and experimental spectrum does not match above 500 in ADC value. The possible reason is that the electron from ^{90}Sr does not have monotonic energy.

$\varepsilon_{\rm col}$	$\overline{q}$	θ	χ^2
0.6	14000	3.0	1.0

Table 4.4: Typical value of parameters for simulation

4.2.3 Transverse diffusion constant

Transverse diffusion at readout strips ($\sigma_{\rm dif}$) is derived from response function of the readout strips. Here, a response function is measured, and then the result is compared with MAGBOLTZ result. MAGBOLTZ is a simulation code which computes drift gas properties such as diffusion constant and drift velocity by numerically integrating the Boltzmann transport equation.

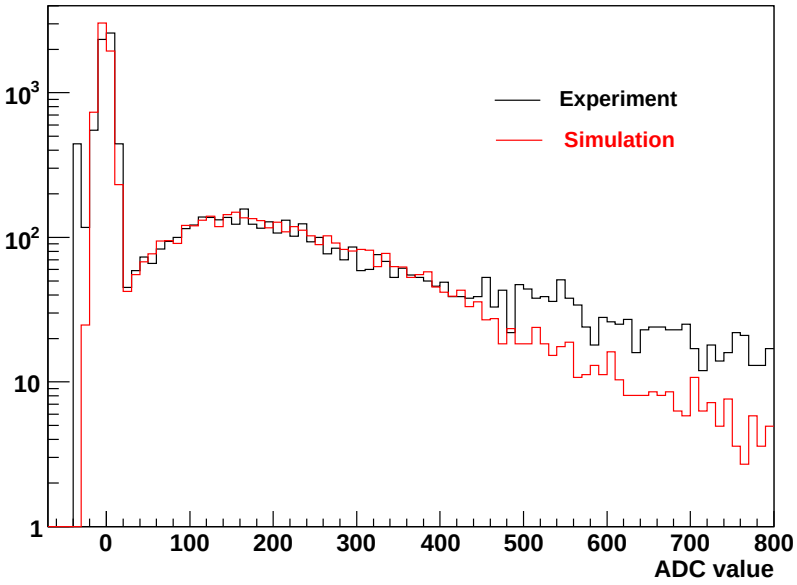

Figure 4.13: Comparison of energy spectrum between experiment and simulation

Test setup

Schematic view of the setup used for measurements of response function is shown in Fig 4.14. Isotope of ^{55}Fe is used as a radiation source. Signal from the bottom side of the last GEM foil is used as a trigger.

The prototype tracker is used in this test. Two types of readout are used here: Double-side readout board with 350μm pitch strips and double-side readout board with effective 700μm pitch strips. In both cases, measurements are performed with top side.

A preamplifier used for readout and the schematic view of the electrical circuit. is shown in Fig 4.15 The preamplifier consists of 2 stages of amplification part. 1MΩ resistor and 1pF capacitance are used as feedback. As a result the time constant of the preamplifier is 1μsec. The second stage amplifies the signal by the factor of 3.2. The total gain of the preamplifier is 3.2V/pC. The preamplifier has differential output.

The preamplifier output is suitable for a flash ADC (RPV-160). RPV-160 has 8 channels and each channel has 8 bits resolution for the full range of $0 \sim -1$V. The sampling rate is 100MHz. A signal is recorded for 640 samples in one event.

A 23m twisted cable is used between the preamplifier and RPV-160.

Result

A response function is shown in Fig 4.16. A fraction of charge on a strip is shown against the distance between the strip center and hit position. The value of $\sigma_{\mathrm{readout}}$ is defined as the standard deviation obtained in a Gaussian fit to the profile histogram of Fig 4.16.

Hit position is determined from the following expression:

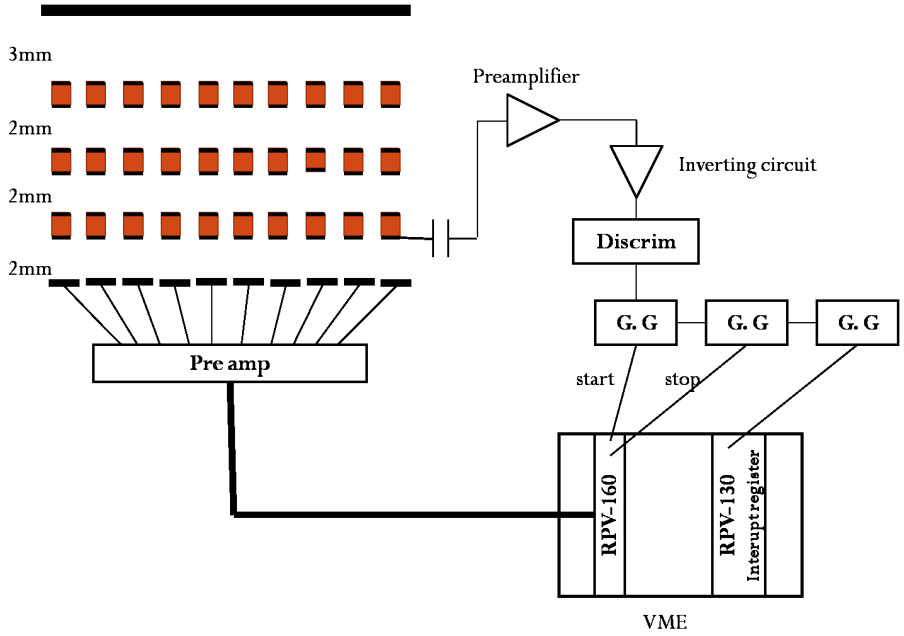

Figure 4.14: Setup of transverse diffusion measurement

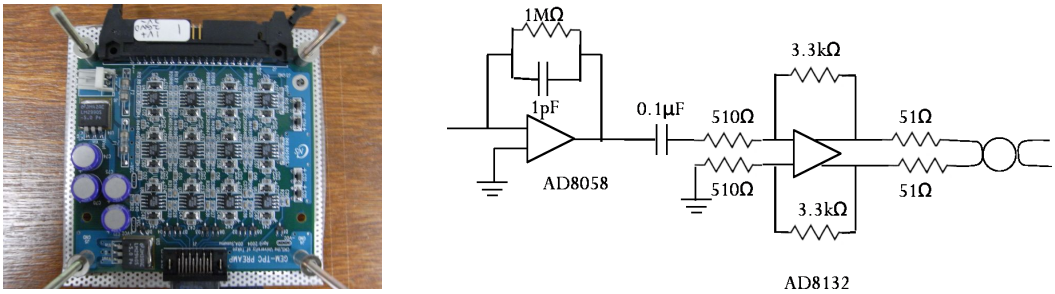

Figure 4.15: A photograph and a schematic view of the electrical circuit of the pre-amplifier

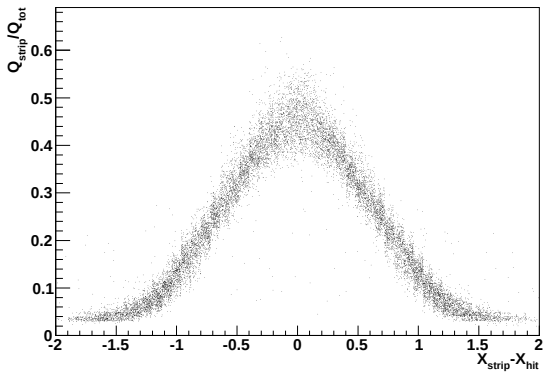

Figure 4.16: A response function of readout strips.

$$X_{\mathrm{hit}} = \frac{\sum Q_j X_j}{\sum Q_j} \tag{4.6}$$

where Q_j charge on the j-th strip
X_j position of the j-th strip

Sum is taken over consecutive strips beyond threshold.

$\sigma_{\mathrm{readout}}$ is measured for 2 setups: P10 with effective 700μm pitch strips and $ArCO_2$ with effective 350μm pitch strips. Gap size and electric field of those setups are summarized in Table 4.5. The results of measurements are shown in Table 4.6, with expected value using MAGBOLTZ simulation. Expected value using MAGBOLTZ is estimated with the following expressions. The diffusion in GEM holes is neglected.

$$\sigma_{\mathrm{read}} = \sqrt{D^2_{\mathrm{drift}} \cdot \frac{d_D}{2} + D^2_{t,i} \cdot (d_{T1} + d_{T1} + d_{T1})} \tag{4.7}$$

where D_{drift} Transverse diffusion constant in drift gap
$D_{t,i}$ Transverse diffusion constant in transfer gap and induction gap

The transverse diffusion constant for various values of electric field calculated with MAGMBOLTZ is shown in Fig 4.17.

The experimental value is larger than the value calculated with MAGBOLZ. The discrepancy is too large to be explained by gas condition. Effect of readout a strip pitch is a possible reason.

gas	pitch	V_{GEM}	$d_{I,T1,T2}$	d_D	E_D	$E_{I,T1,T2}$
P10	700	340V	2mm	3mm	400V/cm	3400V/cm
$ArCO_2$	350	385V	2mm	3.5mm	2500V/cm	3850V/cm

Table 4.5: Details of a triple-GEM configuration in the tests

	P10,700μm pitch	$ArCO_2$, 350μmpitch
Experiment	630	440
MAGBOLTZ	520	220

Table 4.6: Result

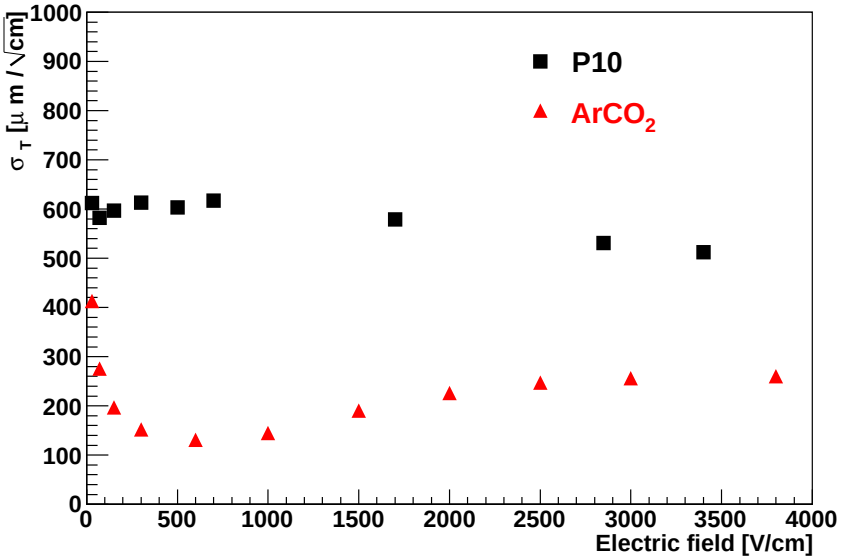

Figure 4.17: Transvers diffusion constant(σ_T) calculated with MAGBOLTZ for P10 and $ArCO_2$

.

4.3 Test of a double-side readout board

As mentioned in section 4.1.2, signal shape and pulse hight of double-side readout board should be checked. In conclusion, the bottom side signal is small and has overshoots, which is not resolved yet. Details are shown below.

4.3.1 Signal shape

Typical signal shape is shown in Fig 4.18. Large overshoots follow the signal. This problem was solved temporarily by coating carbon and acrylic adhesive bond on the readout board. However the overshoots reappeared after some months from the coating. The possible reason is effects of water. The acrylic bond has water absorbability.

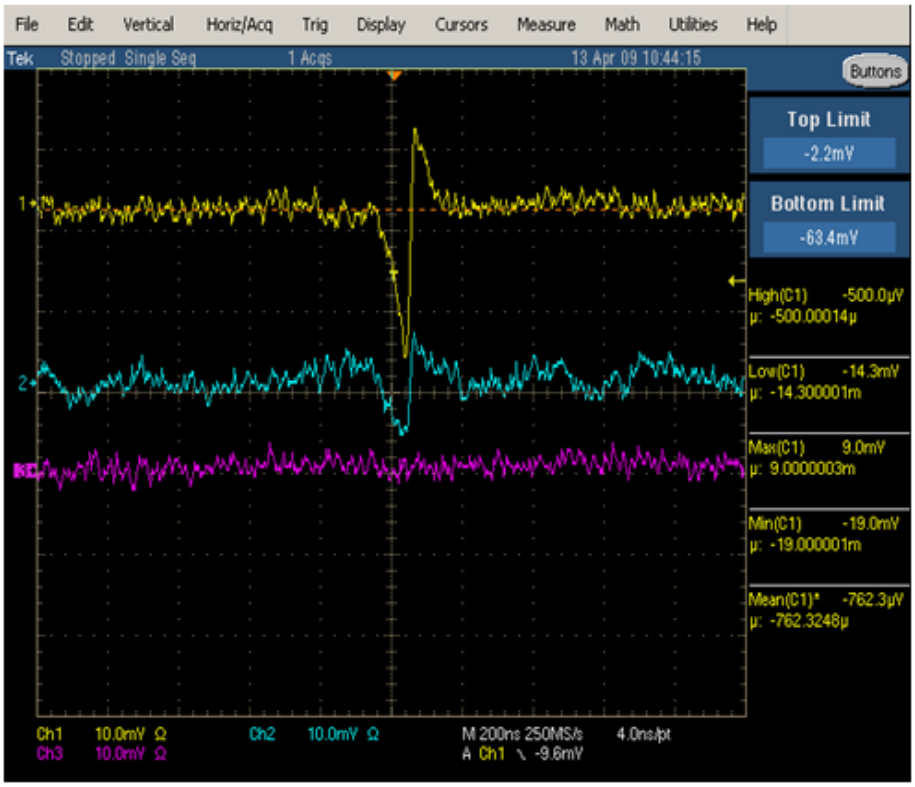

Figure 4.18: Typical bottom side signal shape. Signal of neighboring strips are shown

4.3.2 Charge sharing between top and bottom sides

A geometrical estimation of fraction of charge on top strip(R_{top})is as follows [32].

$$R_{\mathrm{top}} = \frac{\mathrm{w1} \times \mathrm{pitch}}{\mathrm{w2} \times \mathrm{pitch} - \mathrm{w1} \times \mathrm{w2}} \tag{4.8}$$

where
- w1 Width of the top side strips
- w2 Width of the bottom side strips
- pitch Strip pitch

R_{top} is 0.3 for this setup. As the formula neglects the distance between top and bottom layer, top layer collects more charge in reality. Ratio of the charge on top side to the total charge for single side and double side readout are shown in Fig 4.19 and Fig 4.20. The test is performed with P10 and ^{55}Fe. Almost 85% of the electrons fall on the top strips in the double- side case. Decreasing of R_{top} is hard because of the mechanical limitation. The small pulse height will result in low efficiency. That needs to be checked in beam test.

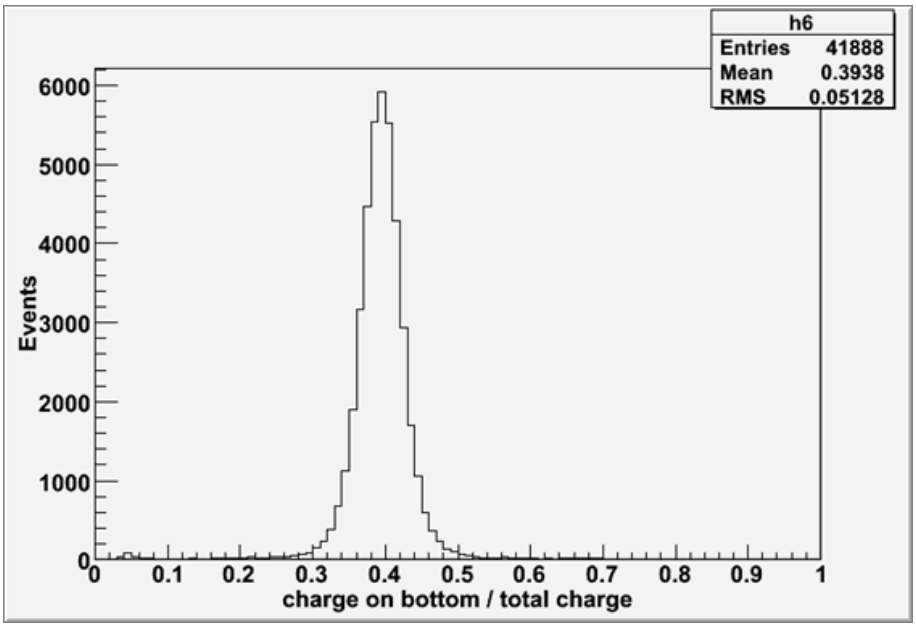

Figure 4.19: The fraction of charge on the top layer to the total for single-side read out

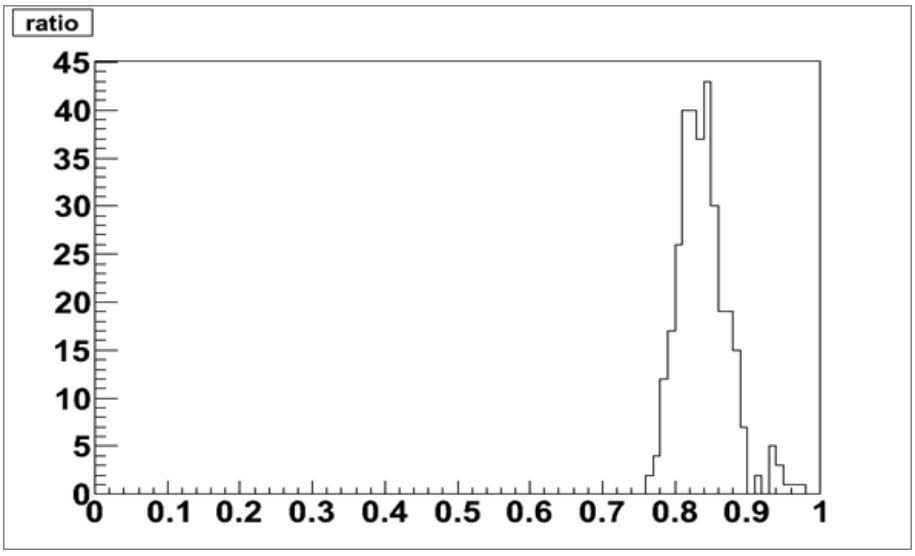

Figure 4.20: The fraction of charge on the top layer to the total for double side read out

Chapter 5

Beamtest

A beam test of the prototype GEM tracker was performed at LNS at Tohoku University. In this chapter, evaluated properties are shown at first , and then setup and result of the beam test is discussed.

5.1 Evaluation properties

Spatial resolution and efficiency of the GEM tracker were evaluated in the beam test: The measurement is performed for the top side and the bottom side of readout board separately.

The goal of spatial resolution is 100μm for angle of 0° to 30°. Originally, the hit position is simply reconstructed from the charge information of strips. However, in that case, the degradation of spatial resolution is expected for tracks which is inclined from normal to the GEM tracker, because such tracks make additional spread in drift gap. Two methods to overcome this degradation is considered.

1. Use narrow drift gap

   Since narrow drift gap makes the spread of charge in drift gap smaller, small angular dependence of spatial resolution can be expected. The major concern is efficiency because narrower drift gap results a small charge.

2. Use wide drift gap and measure arrival time of electrons on strips

   The particle trajectory is reconstructed from timing information like Time Projection Chamber(TPC). Longitudinal diffusion and drift velocity as well as transverse diffusion can affect the accuracy of position determination. The result of MAGBOLTZ simulation is shown in Fig 5.1 and Fig 5.2 for longitudinal diffusion and drift velocity, respectively. Those properties largely depend on an applied electric field. The optimum operational point needs to be determined.

The tested setups are summarized in Table 5.1 and 5.2.

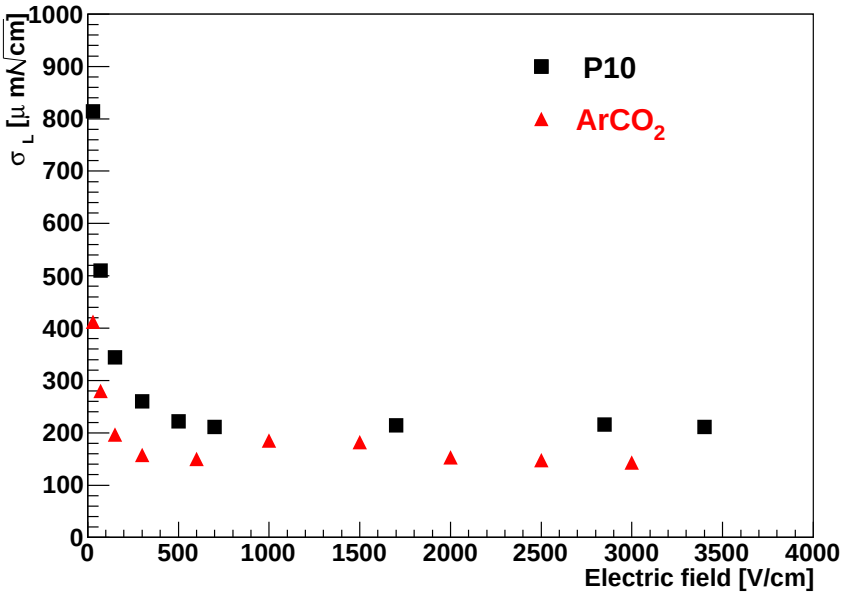

Figure 5.1: Longitudinal diffusion constant calculated with MAGBOLTZ

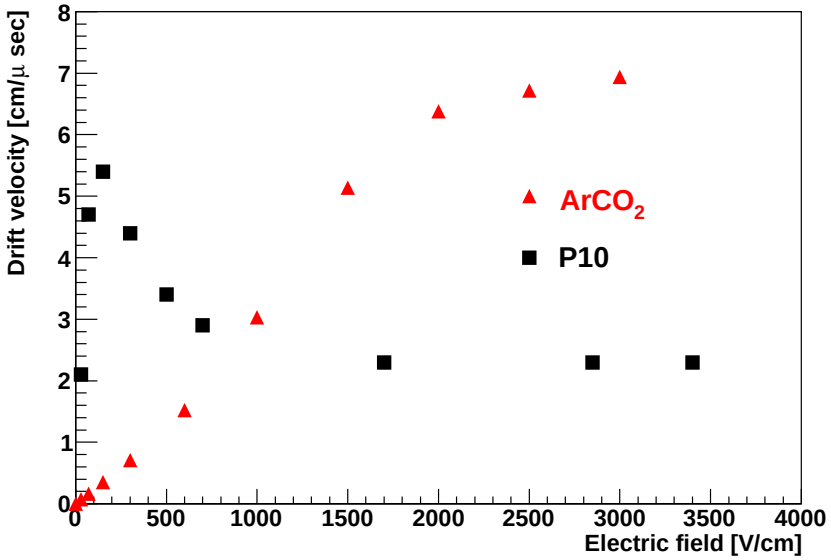

Figure 5.2: Drift velocity calculated with MAGBOLTZ

Table 5.1: Setup of the test for the top side

Gas	Pitch [μm]	d_D [mm]	E_D [V/cm]	Incident angle [deg]
$ArCO_2$	700	11	500	0, 15, 30
$ArCO_2$	350	1	2500	0, 15, 30
$ArCO_2$	350	3	2500	0, 15, 30
$ArCO_2$	350	6	600	0, 15, 30
P10	700	3	1500	0, 15, 30
P10	700	6	1500	0, 15, 30
P10	700	11	500	0, 15, 30

Table 5.2: Setup of the test for the bottom side

Gas	Pitch [μm]	d_D [mm]	E_D [V/cm]	Incident angle[deg]
$ArCO_2$	700	3	2500	0
$ArCO_2$	350	3	2500	0
$ArCO_2$	350	11	500	0
P10	700	3	1500	0
P10	700	11	500	0

5.2 Tested setup

The test setup of the GEM tracker is shown in Fig 5.3. Five scintillators, 3 Silicon Strip Detector and the GEM tracker are aligned along the beam line at LNS.

A coincidence of five scintillators is used to have a beam trigger. Silicon Strip Detector (SSD) is used for tracking.

Table 5.3 summarizes sizes of scintillators and a silicon strip detector.

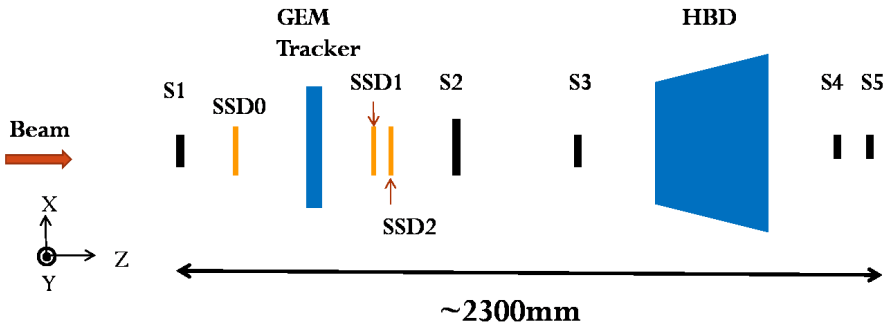

Figure 5.3: The tested setup

Table 5.3: Size of each detector[mm]

S1	S2	S3	S4	S5	SSD
30	50	30	10	10	30

5.2.1 Beam

Beam properties are summarized in Table 5.4.

The schematic view of LNS is shown in Fig 5.4. Electrons are accelerated by LINAC up to 150MeV and STB ring accelerate them up to 1.2GeV.

Bremsstrahlung of accelerated electrons is emitted from the STB ring, and the emitted γ ray is converted to electron-positron pair. Generated positron is used as a beam for tests of the GEM tracker and the momentum of the beam is selected by a dipole magnet.

Table 5.4: Beam properties

Particle	Energy	Spill	Duty factor
positron	660 MeV	7 sec	0.5

5.2.2 Front End Electronics and DAQ

Flash ADC modules and the preamplifiers described in section 4.2.3 are also used here.

We build a DAQ system using VME system. Trigger circuit is shown in Fig 5.5. In this setup, the trigger rate is limited to $\sim$ 20Hz by Flash ADC module.

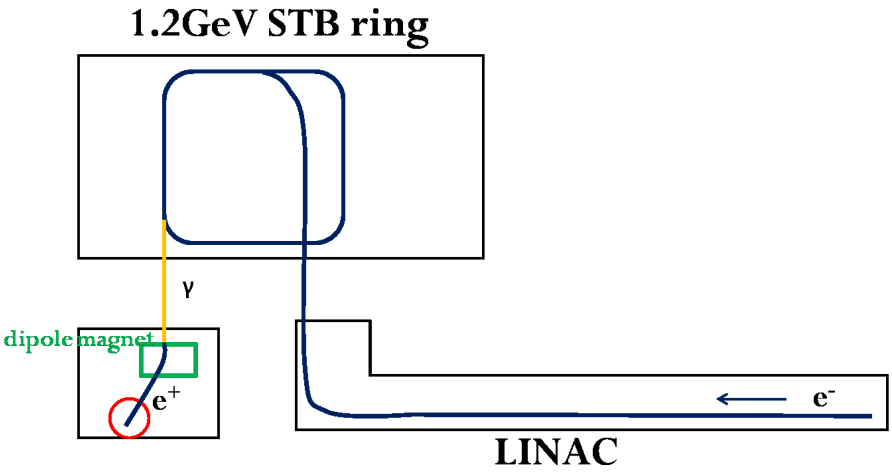

Figure 5.4: The schematic view of LNS: The test is performed at the point indicated by red circle

An ADC module (CAEN V550) and a sequencer module (CAEN V551B) are used for SSD. Charge and timing information of scintillators are collected with ADC (CAEN V792) and TDC (CAEN V775).

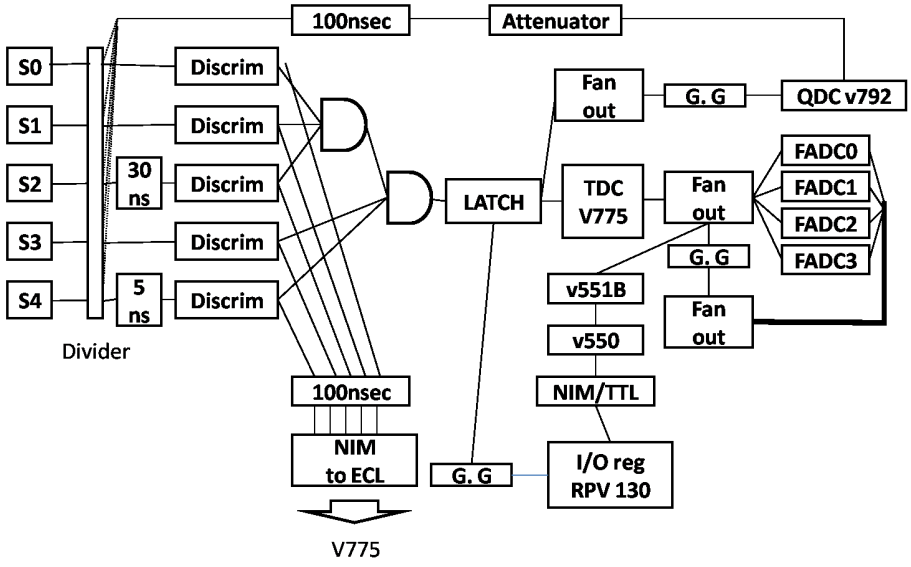

Figure 5.5: Trigger circuit

5.2.3 Scintillator

The acquired spectra of scintillators are shown in Fig 5.6. The landau distribution can be seen.

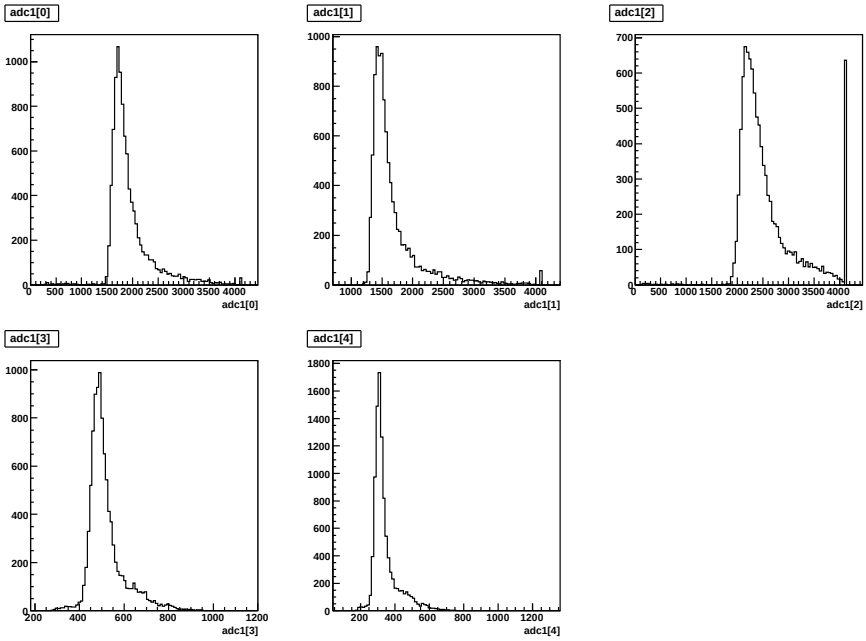

Figure 5.6: The spectrum of scintillators.

5.2.4 Silicon strip detector

Beam position is determined by Silicon Strip Detector (SSD). The basic properties are summarized in Table 5.5.

Table 5.5: SSD properties

Sensitive Area	$30mm \times 30mm$
Thickness	$300\mu m$
Number of Strips	384
Strip pitch	$80\mu m$
Strip width	$60\mu m$
Depletion layer voltage	80V

The SSD has a large common mode noise. Raw ADC values of the SSD need to be converted to significance level, nsigma, for further analysis.

$$nsigma[i] = \frac{ADC[i] - \frac{\sum_j ADC[j]}{N} - Mean[i]}{\sigma[i]} \tag{5.1}$$

where

- i: strip number
- Mean[i]: Mean of $ADC[i] = \frac{\sum_j ADC[j]}{N}$ in pedestal run
- sigma[i]: sigma of $ADC[i] = \frac{\sum_j ADC[j]}{N}$ in pedestal run

The spectrum of nsigma is shown in Fig 5.7. Signals by the beam are well separated from the pedestal peak, which is shown as a large broad peak at the left end. The strip with max value of nsigma is regarded as the hit position of the beam. Fig 5.8 shows a hit map.

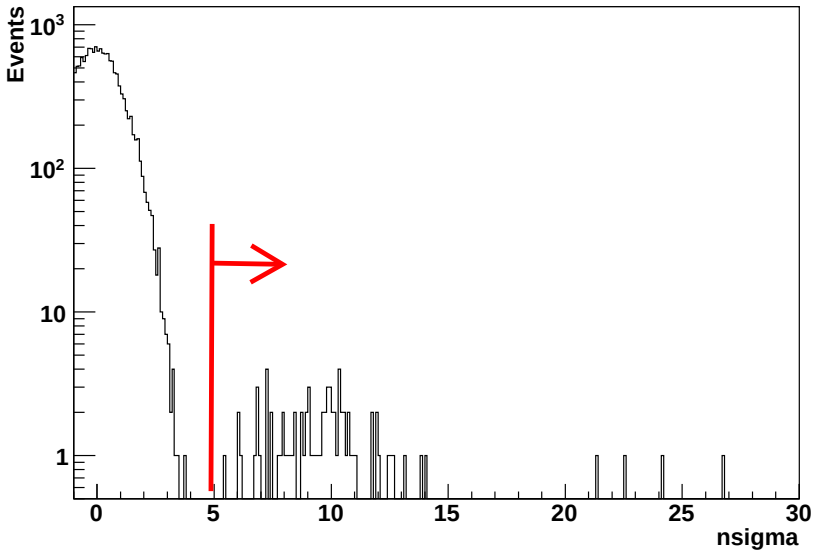

Figure 5.7: Nsigma of SSD

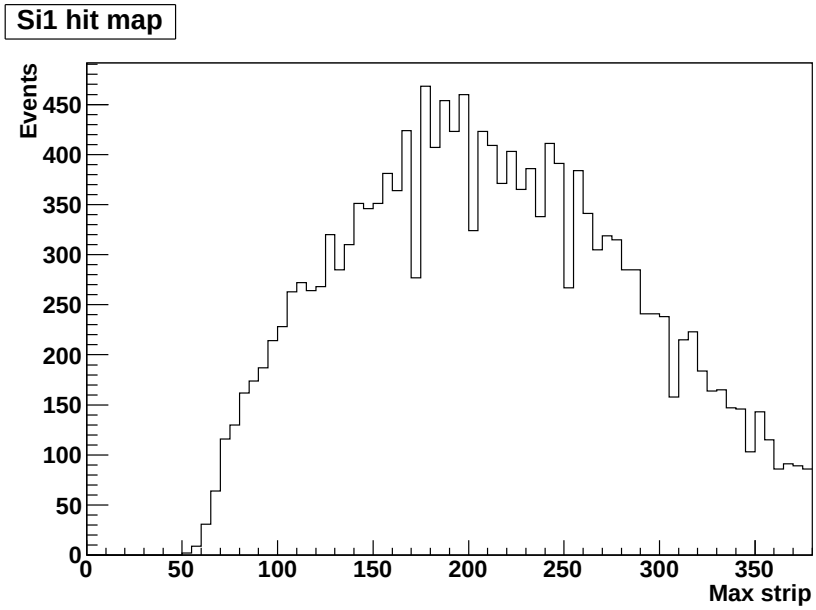

Figure 5.8: Hit map of SSD detector

Cut

Following events are selected for further analysis.

1. All the SSDs have hit strips

2. All the hit strips are clustered within 5 strips

The condition 2 is for killing knocked-out electrons from the SSD or the scintillator. Such knock-out electrons lead to the mis-determination of the beam position. An example of such an event is shown in Fig 5.9

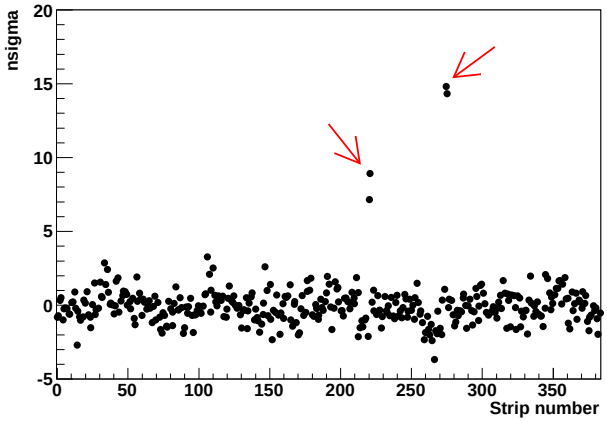

Figure 5.9: A double hit event

Allignment

In the current analysis, the SSD's positions in z-direction are fixed to mechanically designed value, whereas their relative positions in x-direction are optimized in the analysis to match hit positions at both SSDs. Figure 5.10 shows the reconstructed beam angle by SSD0 and SSD1. Only SSD0 and SSD1 were used to interpolate beam tracks at the position of the GEM tracker, because the inclusion of SSD3 for the interpolation leads to 1$\sim$2μm worse residual due to miss alignment of SSD3. The possible reason is the misalignment of SSDs.

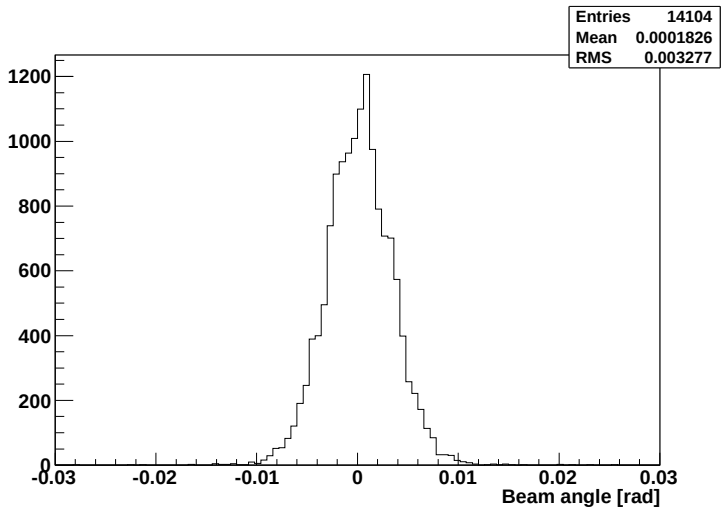

Figure 5.10: Beam angle reconstructed by SSD0 and SSD1 after alignment

5.3 GEM handling in beam test

Our GEM foil has a double-conical-shaped hole and it is known that gain of a double-conical-shaped GEM foil increases with time because of charge-up at hall [24, 33]. Figure 5.11 shows relative pulse height as a function of time. The time constant of charge-up depends on the shape of GEM holes. This phenomenon is understood as follows. When amplification occurs, some fraction of electrons and ions fall on GEM insulator in holes. At the beginning, ions fall on the lower side of holes, while electrons fall on upper side of holes. The electrons and ions on hall wall make additional electric field inside the hole. When the charge-up reaches saturation, a stable gain is obtained.

In the beam test, the high voltage of the GEM tracker was supplied for a few hours before the test. Some test setups did not follow this procedure because of time constrain. However, note that a position sensing detector is not so sensitive to the total charge. Charge-sharing among strips plays an important role as described in the following section.

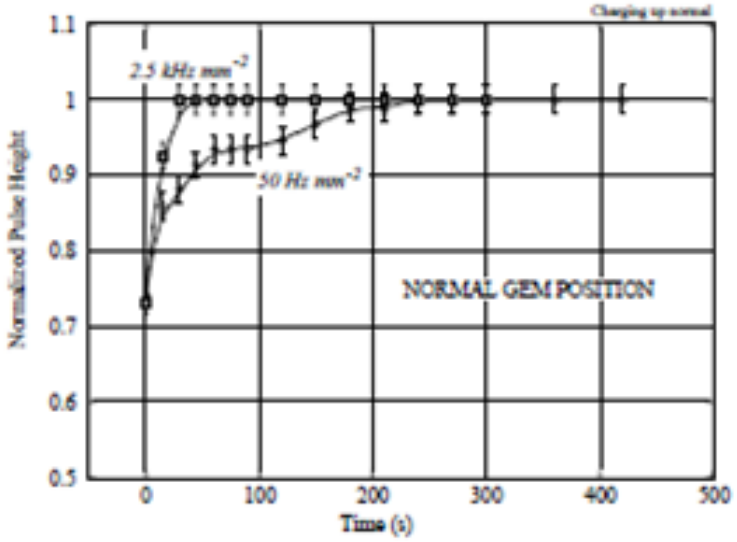

Figure 5.11: Relative pulse height of CERN GEM as a function of time [24].

5.4 Estimation of tracking accuracy

Tracking accuracy of interpolation to GEM from SSD hit positions is evaluated with a brief simulation. The simulation contains spatial resolution and multiple scattering effects. The SSD's spatial resolution (σ_{SSD}) is chosen to reproduce the measured residual of SSD1. Assuming that the spatial resolution of both SSDs are equal, we obtain $\sigma_{\mathrm{SSD}} = 52\mu$m. Table 5.6 compares the residual obtained in the simulation with the measurement. Figure 5.12 compares the residual of the GEM tracker calculated by the simulation as a function of its intrinsic spatial resolution. As a result, the tracking accuracy is estimated to be $\sim 60\mu$m.

Table 5.6: Residual of SSD1 obtained in the simulation and the measurement

Simulation	Experiment
75.5 μm	75.4 μm

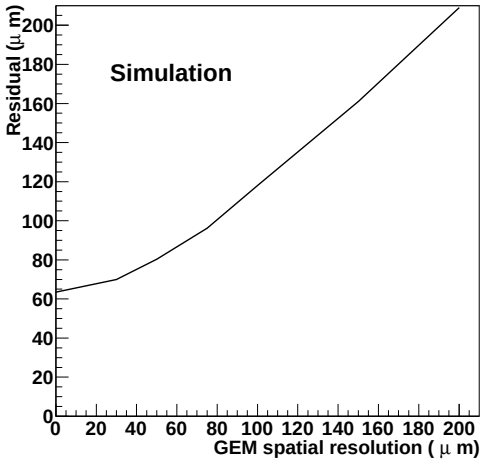

Figure 5.12: The residual of the GEM tracker as a function of its intrinsic spatial resolution

5.5 Analysis results

5.5.1 Pedestal run

Pedestal runs were taken for evaluation of FADC charge offset. The mean V_{ped} and RMS (σ_{ped}) of pedestal per channel are shown in Fig 5.13 for the setups with 350μm and 700μm pitch readout. We can see that there is no sizable difference between them.

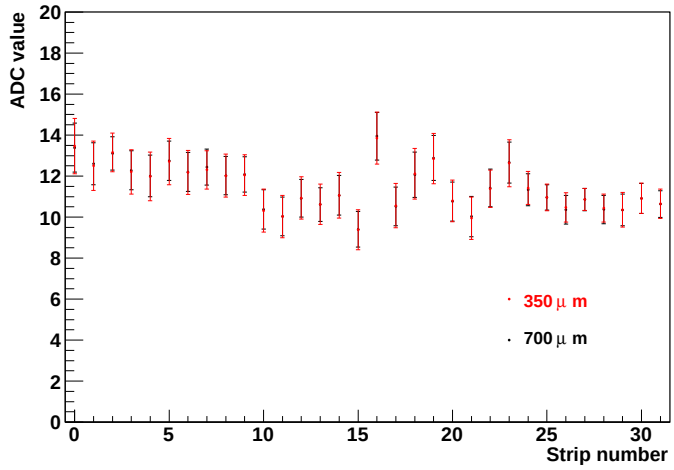

Figure 5.13: Pedestal evaluation

5.5.2 Data and analysis

A typical pulse shape is shown in Fig 5.14. The pulse height increases at first as electrons moving towards readout strips in induction gap, and then decreases with the decay time constant of its readout circuit. The maximum pulse height (V_p) and its arrival time (T_a) of each channel are used for further analysis. The ADC pedestals (V_{ped}) subtracted from V_p. T_a is defined as the time when pulse height exceeds the half of V_p.

After the pedestal subtraction, a program scans through all the strips and find the strip with the maximum V_p, and then recognizes as a cluster including the consecutive strips with $V_p > 3\sigma_N$. Here, $\sigma_N = \sigma_{ped}$. In addition, a cluster is validated if its total charge exceeds $5\sigma_N$.

Inclined tracks causes arrival time difference in a cluster, as shown in Fig 5.15. In the cluster, the strips with the first arrival time (T_1) and the last (T_2) can be identified. Figure 5.16 shows a distribution of $v_d \times (T_2 - T_1)$. Here, v_d is a drift velocity determined by MAGBOLTZ. The right edge of the distribution reproduces the size of drift gap.

Four methods to compute the hit position of the GEM tracker are applied and details are described below, digital-method, COG-method, timing-method 1 and timing-method 2. Timing-method 1 and 2 cannot be used for perpendicular tracks.

Center Of Gravit (COG)-method

In the Center Of Gravity(COG)-method, hit position, X_{COG}, is given by the following expression [34].

$$X_{COG} = \frac{\sum_{i \in cluster} X_i (Q_i - B)}{\sum_{i \in cluster} (Q_i - B)} \tag{5.2}$$

$$B = b \sum_{i \in cluster} Q_i \tag{5.3}$$

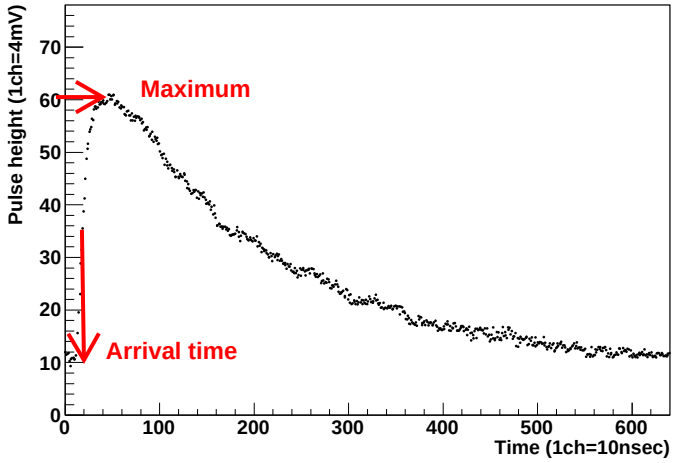

Figure 5.14: A typical pulse shape

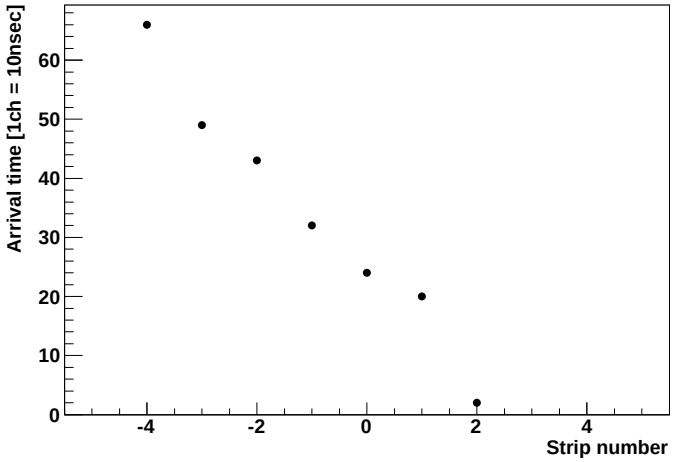

Figure 5.15: Arrival time distribution in a event with the setup $ArCO_2$, 350μm, d_D=6mm, E_D=600V/cm

	Q_i	Charge on the i-th strip
where	X_i	Position of the i-th strip
	b	Constant

The parameter B is a fraction of total charge and is subtracted from Q_i in calculation of center of gravity to eliminate systematic fluctuation caused by total charge fluctuation. b is selected to give a best value of σ_{fit}. Figure 5.17 shows the dependence on b of σ_{fit}.

Digital method

In the digital-method, the hit position, X_{dig}, is given by the following expression.

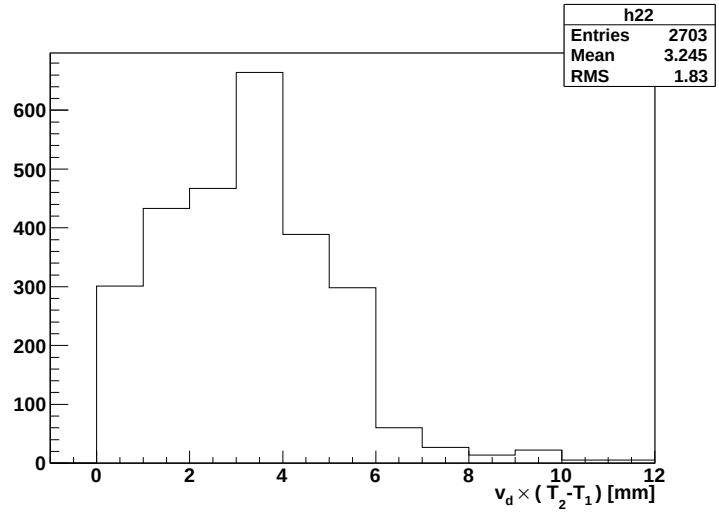

Figure 5.16: Maximum arrival time difference in a cluster multiplied by drift velocity at drift gap with the setup $ArCO_2$, 350μm, d_D=6mm, E_D=600V/cm

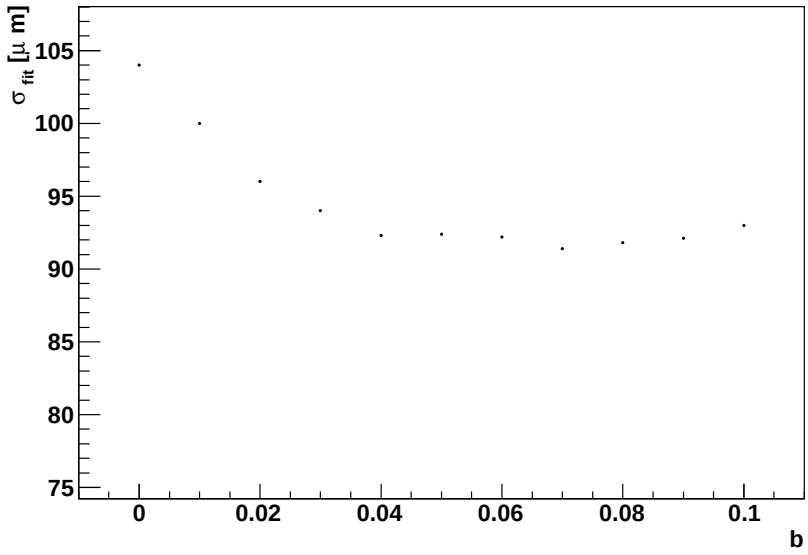

Figure 5.17: σ_{fit} as a function of b. Setup with $ArCO_2$, 350μm pitch, d_D = 1mm, E_D = 2500V/cm

$$X_{dig} = \frac{X_l + X_r}{2} \tag{5.4}$$

where X_l The position of a strip with the smallest strip number
X_r The position of a strip with the largest strip number

The threshold value is selected to give the best value of σ_{fit} with efficiency above 0.97. Figure 5.18 shows the dependence on threshold of σ_{fit} and efficiency.

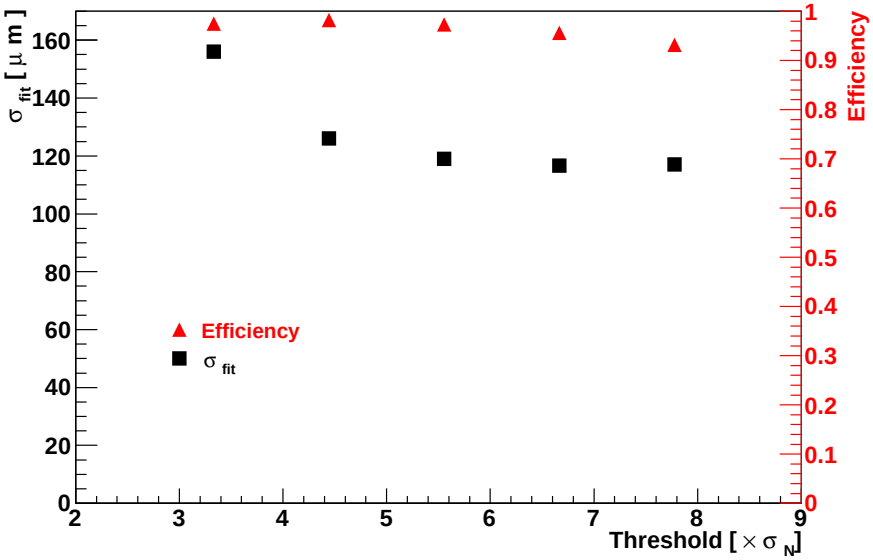

Figure 5.18: σ_{fit} and efficiency as a function of threshold. Setup with $ArCO_2$, 350μm pitch, d_D = 1mm, E_D = 2500V/cm

Timing method 1

The hit position calculated with COG-method and digital-method can be corrected with arrival time information.

Figure 5.19 shows the correlation between the middle arrival time $T_{mid} = (T_{First} + T_{Last})/2$ and the residual σ_{fit} calculated with degital-method.

The obtained correlation was corrected with a linear function. The results after the correction is shown in Fig 5.20.

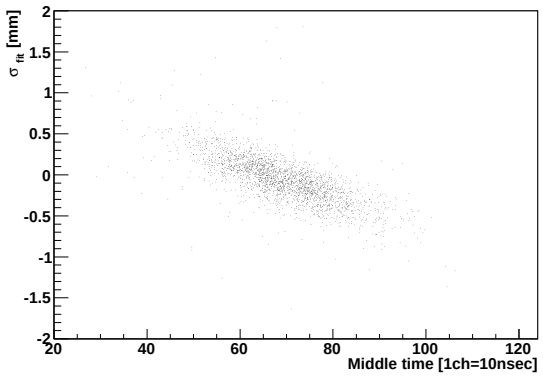

Figure 5.19: Before correction

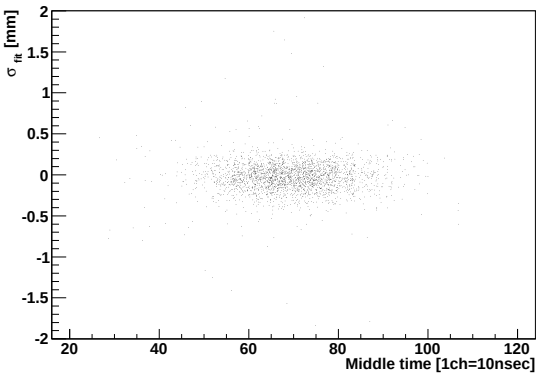

Figure 5.20: After correction

Timing method 2

Next, hit reconstruction is done mainly using timing information. Hit positions were reconstructed in the following way.

1. Check the number of strips above a preset threshold in a cluster. If the number is below 4, the hit position is calculated with digital-method.

2. Find the track. Track position in z-direction at is calculated by multiplying the arrival time with drift velocity of electrons for each strip, We obtained the track in the GEM tracker by fitting those points with a linear function. An example is shown in Fig 5.21. The two edge points are excluded from the fit.

   The reconstructed beam angle is shown in Fig 5.22. The beam angle is well reproduced. The drift velocity is chosen to be 1.2cm/μsec using MAGBOLTZ.

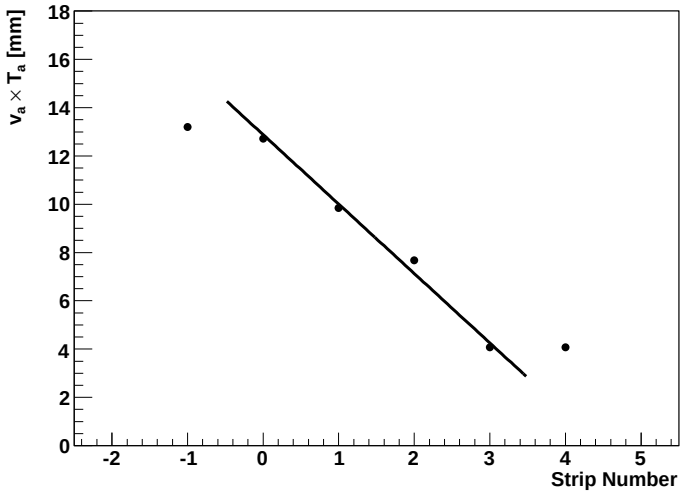

Figure 5.21: An example of a linear fit to $v_d \times T_a$. $ArCO_2$, 700μm pitch,d_D=11mm, E_D=500V/cm

3. Find the hit position. Hit position is defined as the point with z_{ref} as shown in Table 5.7.

Table 5.7: z_{ref} used in Timing method 2

Gas	$ArCO_2$			
Pitch	700μm		350μm	
d_D	11mm		6mm	
E_D	500V/cm		600V/cm	
Angle	15	30	15	30
z_{ref}	8	7.7	6	5.2

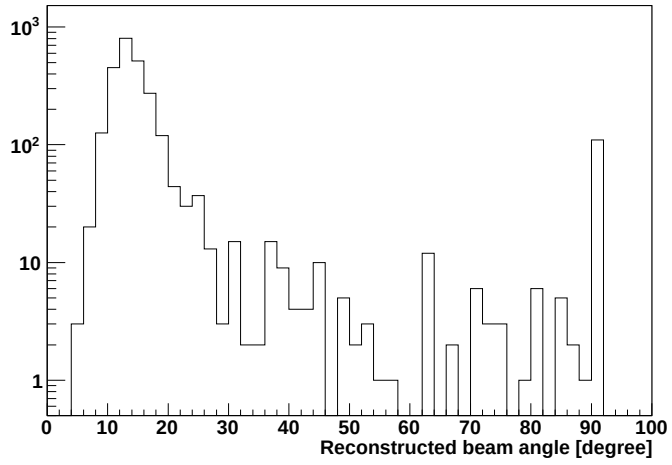

Figure 5.22: Incident angle of reconstructed tracks for 15° inclined track

5.5.3 Alignment of the GEM tracker to the SSDs

The position of the GEM tracker in z-direction is determined to minimize its residual. Figure 5.23 shows the residual as a function of the tracker position calculated by design value. The position indicated with black arrow is the center of drift gap. The difference needs to be investigated.

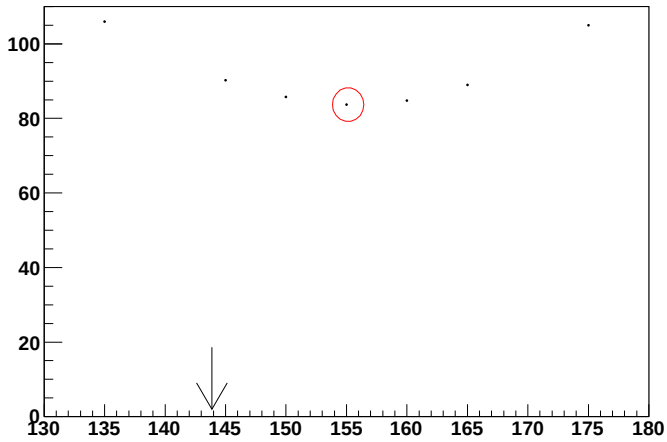

Figure 5.23: Residual of GEM tracker as a function of virtually placed GEM position in a program

5.5.4 Total charge, S/N ratio and uniformity

Figure 5.24 shows total charge obtained by Flash ADC as a function of hit position obtained with the SSDs. Since total charge is clearly smaller in the region above 8mm, tracks in this region are excluded for further analysis. The mean value of total cluster charge varies less than 1% for the selected region.

Figure 5.25 shows the distribution of the total cluster charge of the GEM tracker. The signal/noise ratio, defined as the ratio of total cluster charge to the rms of a GEM strip noise, is around 50. The signal/noise ratio is negligible compared to the first term in eq (4.1). Thus the spatial resolution is mainly determined by physics processes in drift gap and effects of strip pitch.

5.5.5 Time calibration

Channel dependence of timing offset for Flash ADC is also checked as shown in Fig 5.26. The fluctuation is less than 4ch.

5.5.6 Spatial resolution and efficiency

Using a track position provided by SSDs, efficiency and spatial resolution is evaluated. Figure 5.27 shows a typical residual distribution between the hit position of the GEM tracker and SSD interpolated position. A Gaussian fit to the distribution provides a

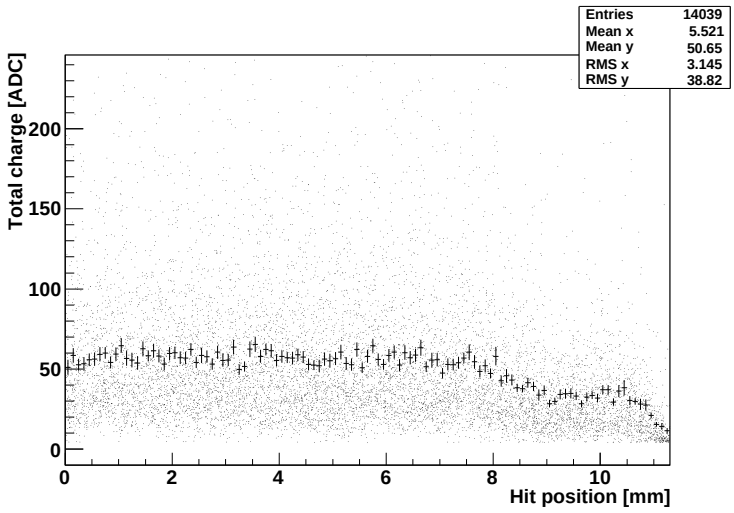

Figure 5.24: Total cluster charge vs. hit position with $ArCO_2$, 350μm, d_D:1mm, E_D: 2500V/cm

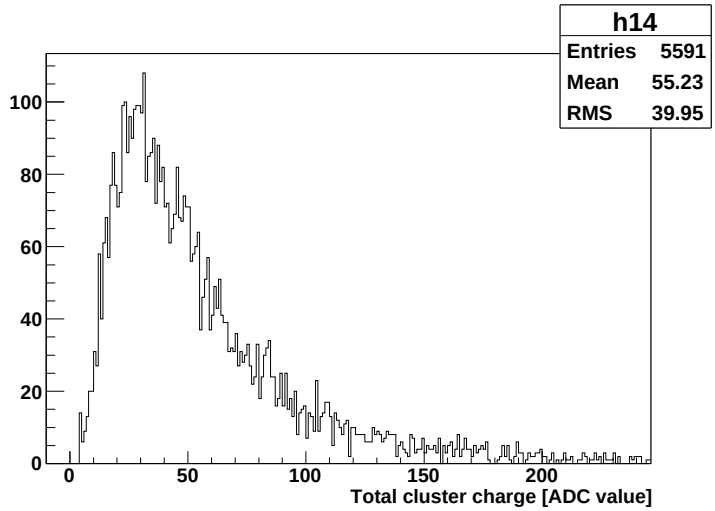

Figure 5.25: Total cluster charge measured with $ArCO_2$, 350μm, d_D:1mm, E_D: 2500V/cm

standard deviation σ_{fit}. Efficiency calculation is done for events, which are found in 5 σ_{fit}. Spatial resolution is calculated by subtracting the tracking accuracy from σ_{fit}.

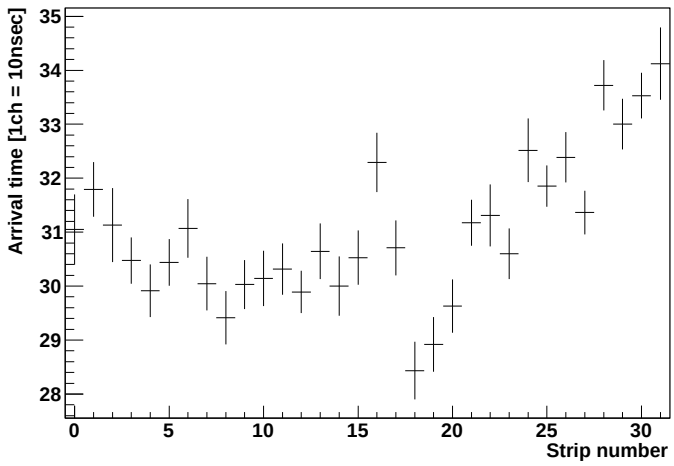

Figure 5.26:

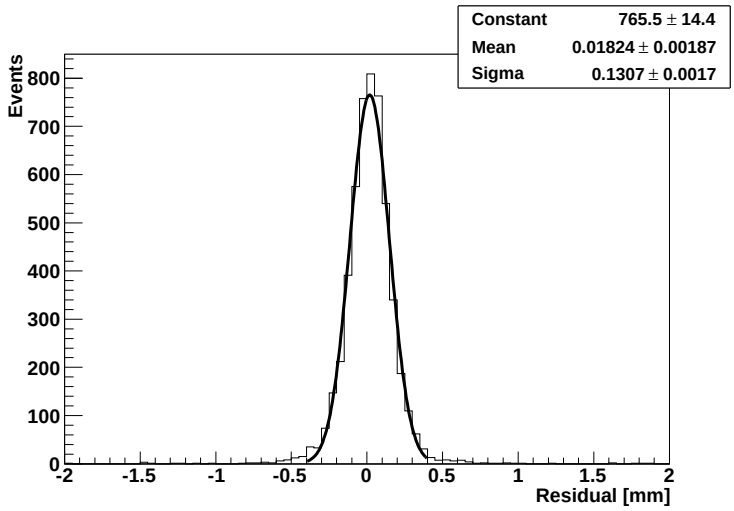

Figure 5.27: Typical residual distribution

Top side

Several setups are tested and only good setups are discussed below. Table 5.8 shows the setup which achieves spatial resolution less than 200μm for 15° inclined track. The spatial resolution is plotted against the track's angle for those setups in Fig 5.28-5.31. When only charge information is used, the degradation of spatial resolution with incidence angle is smaller for narrower drift gap. However, the spatial resolution for a 30° tracks is 270μm even with d_D = 1mm. That is far beyond our goal. We can see that timing-methods improves σ_{fit} for the setup 3 and 4. Timing methods become effective with the setup having large number of hit strips and large arrival time difference in a cluster. From this point of view, setup 1 and 2 are not suitable for timing methods because they have narrow

drift gaps and large drift velocity. In the end, the best spatial resolution for 30° inclined beam is 170μm with the setup 3 using timing method 2.

However, timing method 2 suffers small detection efficiency as shown in Table 5.9, while other methods achieve the efficiency above 0.97. Figure 5.32 shows a typical residual distribution obtained with timing method 2. The distribution has tails on both sides of the peak. Two types of events can make the tails, when the track reconstruction is failed. Another is when the digital method is applied and timing information is not used..

We can also see that COG method degrades faster than digital-method with an increase of incident angle. Figure 5.33 shows an example of charges recorded using setup 4 with 15° inclined beam. The charge on each strip is fluctuated largely. Therefore including this information simply degrades the spatial resolution. The possible reason of the double-peak distribution is the fluctuation of electron cluster size in drift gap.

Table 5.8: Setup with the residual better than 200μm

No.	Gas	Pitch [μm]	d_D [mm]	E_D [V/cm]
1	$ArCO_2$	700	11	500
2	$ArCO_2$	350	6	600
3	$ArCO_2$	350	3	2500
4	$ArCO_2$	350	1	2500

Table 5.9: Detection efficiency of setup 3 and setup 4 using timing method 2 for track finding

	Setup 3		Setup 4	
	15°	30°	15°	30°
Efficiency	0.92	0.85	0.97	0.85

Bottom side

Table 5.10 shows the efficiency and spatial resolution of the bottom side. The efficiency above 0.97 is achieved with d_D = 11mm. Thus, wide drift gap is essential to achieve the full detection efficiency on the bottom side.

Table 5.10: Spatial resolution and efficiency of bottom side

Gas	Pitch [μm]	d_D [mm]	E_D [V/cm]	Resolution	Efficiency
P10	700μm	3	1500	240	0.75
		11	500	154	0.98
$ArCO_2$	350	3	2500	124	0.86
		11	500	110	0.97

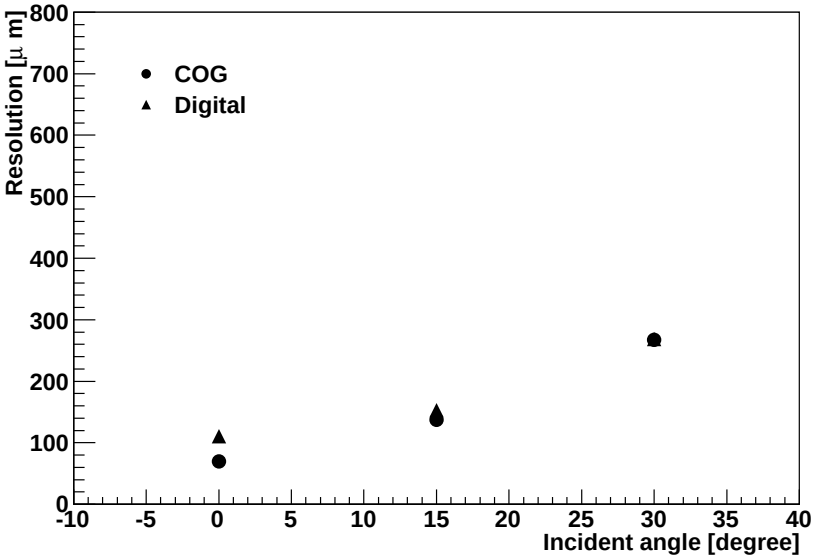

Figure 5.28: $ArCO_2$, 350mum pitch, $d_D = 1mm$, $E_D = 2500V/cm$

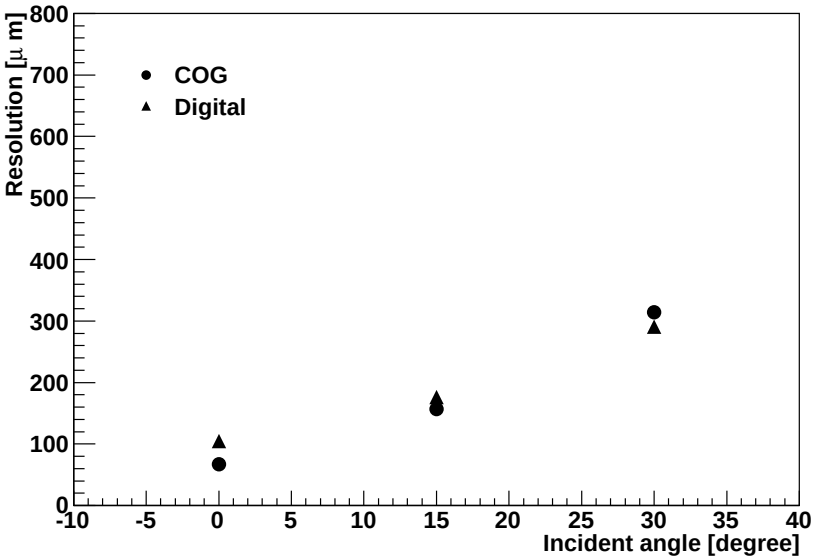

Figure 5.29: $ArCO_2$, 350mum pitch, $d_D = 3mm$, $E_D = 2500V/cm$

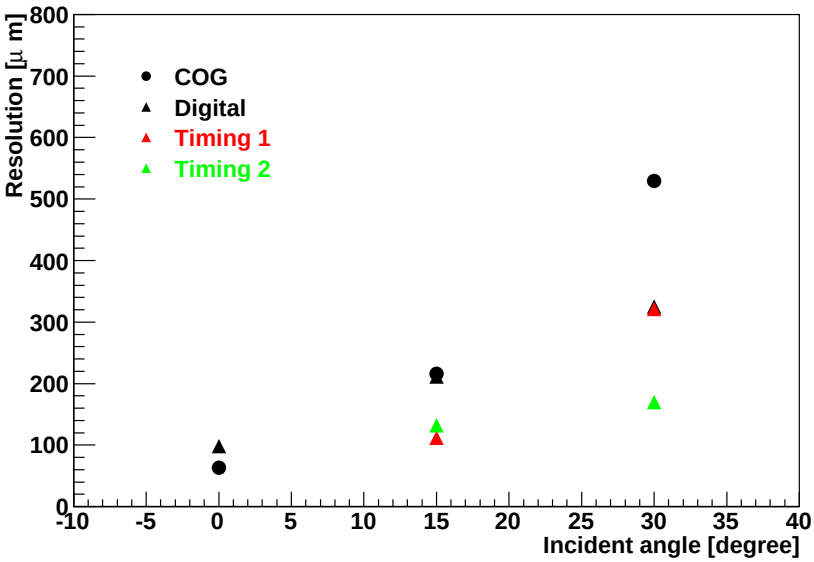

Figure 5.30: $ArCO_2$, 350mum pitch, $d_D = 6mm$, $E_D = 600V/cm$

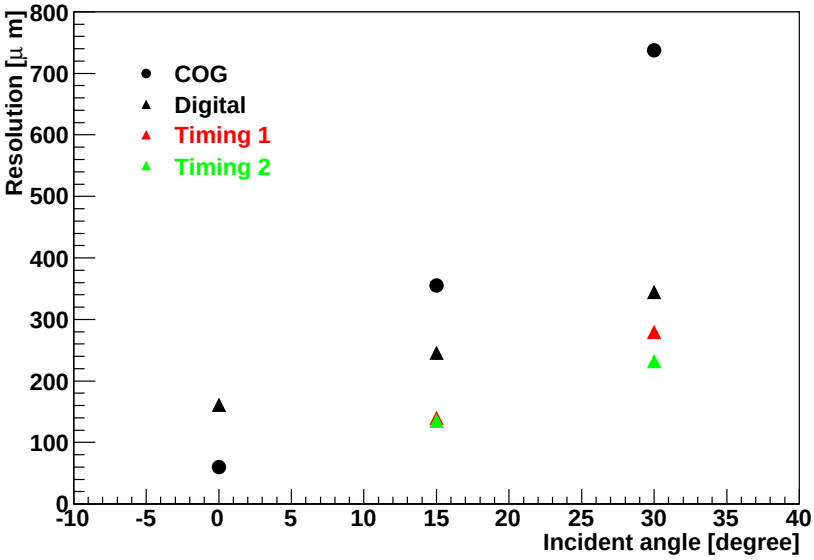

Figure 5.31: $ArCO_2$, 700mum pitch, $d_D = 11mm$, $E_D = 500V/cm$

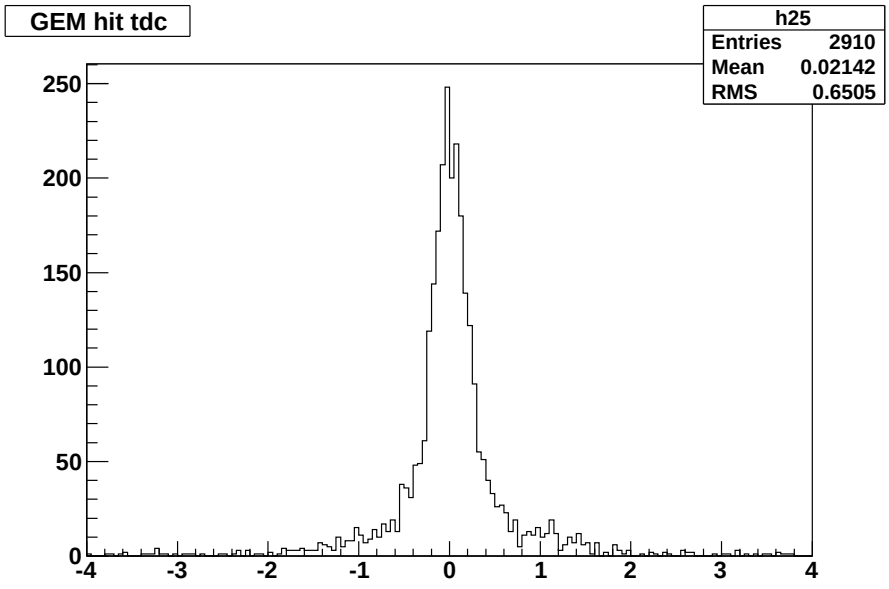

Figure 5.32: A typical residual distribution using timing method2

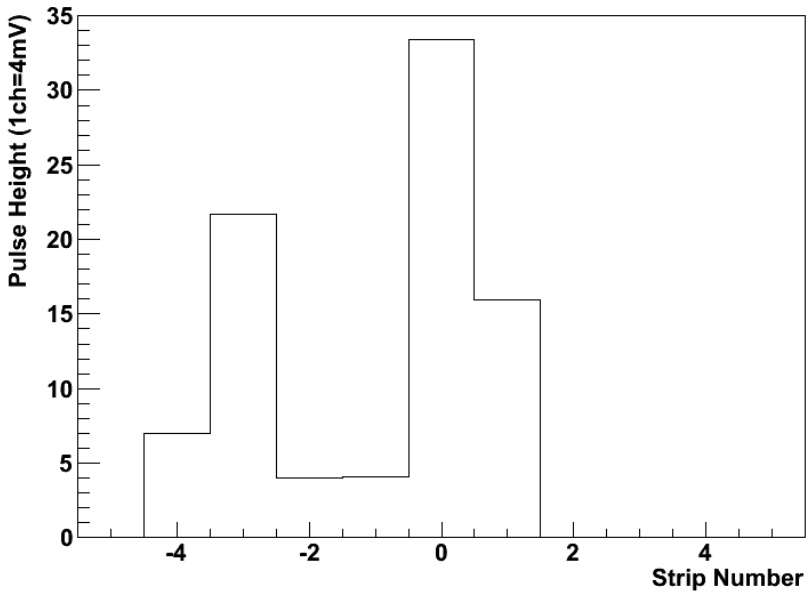

Figure 5.33: Typical charge profile for a 15° inclined track, recorded with setup 4

Chapter 6

Conclusion

A prototype GEM tracker was constructed for J-PARC E16 experiment. The required spatial resolution is 100 μm for tracks of incident angle of 0° to 30°.

Two methods to overcome the problem of a resolution degradation for non-perpendicular tracks is considered.

1. Use narrow drift gap
2. Use wide drift gap and measure arrival time of electrons on strips

As a result, the best spatial resolution for 30° inclined beam is 170μm with the following setup.

Gas	Pitch	d_D	E_D	Method
$ArCO_2$	350μm	6mm	600V/cm	Timing method 2

However timing method 2 suffers small detection efficiency. The R&D activity is still on-going to improve the spatial resolution and efficiency.

Acknowledgement

I would like to express my gratitude to Prof. K. Ozawa, who has led me to this interesting field of science. I am also grateful to his continuous support and guidance at every stage of this work.

I am much obliged to Prof. H. Enyo, Dr. M. Sekimoto, Dr. S. Yokkaichi and Dr. K. Aoki. Their meticulous comments and advice were enormous help to me. I learned the attitude towards experiment from them.

I would like to thank Prof. H. Hamagaki and Dr. T. Gunji. Their advice on beam test helped me a lot. I am also grateful to Mr. Y. Hori and Mr. T. Tsuji. Their help was indispensable to the operation of SSD.

Special thanks are due to Tohoku LNS group, in particular Dr. T. Ishikawa. He gave me a lot of useful information on the beam test.

Finally, I express my thanks to members of Ozawa group. I am grateful to Mr. K. Utsunomiya for construction of DAQ. I also appreciate him for his friendship and fruitful discussion. I would like to thank Mr. Y. Komatsu and Mr. S. Masumoto for their advice and support.

Bibliography

[1] D.J. Gross, Proc. Nat Acad. Sci. 102 (2005) 9099

[2] H.D. Politzer, Proc. Nat Acad. Sci. 102 (2005) 7789

[3] F. Wilczek, Proc. Nat Acad. Sci. 102 (2005) 8403

[4] C. Amsler, Physics Letters B 667 (2008) 1

[5] Y. Numbu and G. Jona-Lasinio, Phys. Rev. 122 (1961a) 345

[6] Y. Numbu and G. Jona-Lasinio, Phys. Rev. 124 (1961b) 246

[7] E.G. Drukarev and E.M. Levin, Prog. Part. Nucl. Phys. 27 (1991) 77

[8] G.E. Brown and M. Rho, Phys. Rev. Lett. 66 (1991) 2720

[9] T. Hatsuda and S.H. Lee, Phys. Rev. C. 46 (1992) R34

[10] G. Chanfray, R. Rapp and J. Wambach, Phys. Rev. Lett. 76 (1996) 368

[11] J.I. Kapusta and E.V. Shuryak, Phys. Rev. D. 49 (1994) 4694

[12] D. Adamova et al., Phys. Lett B 666 (2008) 425

[13] S. Damjanovic, Nucl. Phys. A 783 (2007) 327c

[14] M. Naruki et al., Phys. Rev. Lett, 96 (2006) 092301

[15] R. Muto et al., Phys. Rev. Lett, 98 (2007) 042501

[16] M.H. Wood, Phys. Rev. C. 78 (2008) 015201

[17] D. Trnka et al, Phys. Rev. Lett. 94 (2005) 192303

[18] T. Ishikawa et al, Phys. Lett B 608 (2005) 215

[19] R.S. Hayano and T. Hatsuda, arXiv:0812.1702[nucl-ex]

[20] S. Leupold, V. Metag and U. Mosel, arXiv:0907.2388v1[nucl-th]

[21] B.A. Mecking et al., Nucl. Instr. and Meth. A 503 (2003) 513

[22] `http://j-parc.jp/NuclPart/pac_0606/pdf/p16-Yokkaichi_2.pdf`

[23] F. Sauli, Nucl. Instr. and Meth. A 386 (1997) 531

[24] C. Altunbas et al., Nucl. Instr. and Meth. A 490 (2002) 177

[25] B. Ketzer et al., IEEE Trans. Nucl. Sci., vol. 47 No. 5 (2002) 2002

[26] M. Kobayashi, Nucl. Instr. and Meth. A 562 (2006) 136

[27] F. Sauli, CERN 77-09 (1977)

[28] M.M. Morii, T. Taniguchi and Y. Fukushima, KEK Preprint 88-80 (1980)

[29] A. Buzulutskov et al. Nucl. Instr. and Meth. A 443 (2000) 164

[30] G.D. Alkhazov, Nucl. Instr. and Meth 89 (1970) 155

[31] H. Fischle, Nucl. Instr. and Meth. A 301 (1991) 202

[32] A. Bressan et al., Nucl. Instr. and Meth. A 425 (1999) 254

[33] O. Bouianov, Nucl. Instr. and Meth. A 450 (2000) 277

[34] G. Charpak et al., Nucl. Instr. and Meth. 148 (1978) 471